The Astrophysical Journal Supplement Series, 234:19 (25pp), 2018 February https://doi.org/10.3847/1538-4365/aaa29b

The Impact of Nuclear Reaction Rate Uncertainties on the Evolution of Core-collapse Supernova Progenitors

C. E. Fields[1,2,6], F. X. Timmes[2,3], R. Farmer[3,4], I. Petermann[2,3], William M. Wolf[3,5], and S. M. Couch[1,2]
[1] Department of Physics and Astronomy, Michigan State University, East Lansing, MI 48824, USA; fieldsc9@msu.edu
[2] Joint Institute for Nuclear Astrophysics—Center for the Evolution of the Elements, USA
[3] School of Earth and Space Exploration, Arizona State University, Tempe, AZ, USA
[4] Anton Pannenkoek Institute for Astronomy, University of Amsterdam, NL-1090 GE Amsterdam, The Netherlands
[5] Department of Physics, University of California, Santa Barbara, CA 93106, USA
Received 2017 October 31; revised 2017 December 15; accepted 2017 December 16; published 2018 January 25

Abstract

We explore properties of core-collapse supernova progenitors with respect to the composite uncertainties in the thermonuclear reaction rates by coupling the probability density functions of the reaction rates provided by the STARLIB reaction rate library with MESA stellar models. We evolve 1000 models of $15M_{\odot}$ from the pre-main sequence to core O-depletion at solar and subsolar metallicities for a total of 2000 Monte Carlo stellar models. For each stellar model, we independently and simultaneously sample 665 thermonuclear reaction rates and use them in a MESA in situ reaction network that follows 127 isotopes from ^{1}H to ^{64}Zn. With this framework we survey the core mass, burning lifetime, composition, and structural properties at five different evolutionary epochs. At each epoch we measure the probability distribution function of the variations of each property and calculate Spearman rank-order correlation coefficients for each sampled reaction rate to identify which reaction rate has the largest impact on the variations on each property. We find that uncertainties in the reaction rates of ^{14}N(p, γ)^{15}O, triple-α, ^{12}C(α, γ)^{16}O, ^{12}C(^{12}C,p)^{23}Na, ^{12}C(^{16}O, p)^{27}Al, ^{16}O(^{16}O,n)^{31}S, ^{16}O(^{16}O, p)^{31}P, and ^{16}O(^{16}O,α)^{28}Si dominate the variations of the properties surveyed. We find that variations induced by uncertainties in nuclear reaction rates grow with each passing phase of evolution, and at core H-, He-depletion they are of comparable magnitude to the variations induced by choices of mass resolution and network resolution. However, at core C-, Ne-, and O-depletion, the reaction rate uncertainties can dominate the variation, causing uncertainty in various properties of the stellar model in the evolution toward iron core-collapse.

Key words: stars: abundances – stars: evolution – stars: interiors – supernovae: general

1. Introduction

Core-collapse supernova (SN) explosions are one possible fate of a star with a zero-age main-sequence mass of $M \gtrsim 9M_{\odot}$ (e.g., Woosley et al. 2002; Woosley & Heger 2007; Farmer et al. 2015). The structure of the progenitor at the time of explosion can lead to a large variety of observed transient phenomena (e.g., Van Dyk et al. 2000; Ofek et al. 2014; Smith et al. 2016).

For progenitors experiencing mass loss, stellar winds may strip the H-rich envelope, and possibly some of the He-rich envelope, prior to core-collapse (e.g., Smith 2014; Renzo et al. 2017). Explosions of these stars are characterized by an absence of hydrogen absorption features and weak or non-existent absorption lines of silicon in their spectra (Smartt 2009, 2015; Dessart et al. 2011; Reilly et al. 2016; Sukhbold et al. 2016). Progenitors with most of the H-rich envelope present at the end of their life are characterized as Type II supernovae, which can be sub-divided into multiple classes based on light-curve and spectral properties (Filippenko 1997; Wang & Wheeler 2008; Jerkstrand et al. 2015).

In some cases, a massive star with sufficient rotational energy at core-collapse can produce a rapidly rotating, highly magnetic proto-neutron star capable of leading to a significantly enhanced energetic transient. Such a scenario has been postulated to explain the most energetic supernova observed to date, ASASSN-15lh (Chatzopoulos et al. 2016b; Chen et al. 2016; Sukhbold & Woosley 2016; Dong et al. 2016), although Leloudas et al. (2016) offers on an alternative hypothesis on the nature of ASASSN-15lh.

Alternatively, a massive star may undergo iron core-collapse but the resulting shocks are insufficient to unbind the star, leading to accretion onto the nascent proto-neutron star pushing it past its maximum mass. These "failed supernovae" (e.g., O'Connor & Ott 2011) can produce stellar-mass black holes at the rate suggested by the detection of GW150914, GW151226, and GW170104 (Abbott et al. 2016a, 2016b, 2017), although a broad consensus on which massive stars produce black holes has not yet been reached (Timmes et al. 1996; Fryer & Kalogera 2001; Heger et al. 2003; Eldridge & Tout 2004; Zhang et al. 2008; Ugliano et al. 2012; Clausen et al. 2015; Kruckow et al. 2016; Müller et al. 2016; Sukhbold et al. 2016, 2017; Woosley 2016; Limongi 2017).

For more massive progenitors, pair-instability leads to a partial collapse, which in turn causes runaway burning in the carbon–oxygen core (Fowler & Hoyle 1964; Barkat et al. 1967; Rakavy & Shaviv 1967; Rakavy et al. 1967; Fraley 1968). A single energetic burst from nuclear burning can disrupt the entire star without leaving a black hole remnant behind to produce a pair-instability supernova (Ober et al. 1983; Fryer et al. 2001; Kasen et al. 2011; Chatzopoulos et al. 2013). Alternatively, a series of bursts can trigger a cyclic pattern of nuclear burning, expansion, and contraction, leading to a pulsational pair-instability supernova that leaves a black hole remnant (Barkat et al. 1967; Woosley & Heger 2007; Chatzopoulos & Wheeler 2012; Limongi 2017; Woosley

[6] NSF Graduate Research Fellow, Ford Foundation Predoctoral Fellow.

2017). A variety of outcomes is possible depending on the star's mass and rotation.

At the heart of these evolutionary pathways are nuclear reaction rates. These rates regulate the evolution of the star and can significantly modify the stellar structure of the progenitor star at the end of its life. Uncertainties in the reaction rates can have the direct consequence of differences in the nucleosynthesis and explosion properties (Rauscher et al. 2002, 2016; Woosley & Heger 2007; Sukhbold et al. 2016).

Most reaction rate libraries provide recommended nuclear reaction rates based on experiment (when possible) or theory. Examples include CF88 (Caughlan & Fowler 1988), NACRE (Angulo et al. 1999; Xu et al. 2013), JINA REACLIB (Cyburt et al. 2010), and STARLIB (Sallaska et al. 2013). STARLIB takes the additional step of providing the median or recommended thermonuclear reaction rate *and* the factor uncertainty (*f.u.*) as a function of temperature. The factor uncertainty is an estimate of the uncertainty associated with a reaction rate at a given temperature given the available nuclear physics data. Reaction rates based on Monte Carlo (Longland et al. 2010; Longland 2012; Iliadis et al. 2015, 2016) or Bayesian theory (Iliadis et al. 2016; Gómez Iñesta et al. 2017) generate probability density functions (PDFs) to provide a final *median* rate and a temperature-*dependent* uncertainty. The availability of formally derived temperature-dependent uncertainties allows statistically rigorous studies on the impact of the composite uncertainty on stellar models.

Studies of reaction rate sensitivity have been considered for models of X-ray bursts (Cyburt et al. 2016) and massive stars through core He-burning (West et al. 2013) and for *s*-process nucleosynthesis (Nishimura et al. 2017). In some of these and similar studies, temperature-*independent* estimates of the reaction rate uncertainties are applied as constant multiplicative factors on the recommended rate at all temperatures. This method can lead to an under- or overestimate of the reaction rate for different stellar temperatures. Another common approximation is "post-processing" of thermodynamic trajectories from stellar models (e.g., Magkotsios et al. 2010; Rauscher et al. 2016; Harris et al. 2017), which also usually use a constant multiplicative factor at all temperature points. Post-processing thermodynamic trajectories neglect the feedback of the changes in the reaction rates on the underlying stellar model.

Fields et al. (2016, hereafter F16) addresses some of the shortcomings of these approximations by using a Monte Carlo stellar model framework with temperature-dependent uncertainties on the reaction rates from STARLIB. Specifically, it is used on $3M_{\odot}$ stellar models evolved from the pre-main sequence to the first thermal pulse. Each of the 1000 models uses one set of reaction rates generated from the reaction rate PDFs. These Monte Carlo stellar models probed the effect of reaction rate uncertainties on the structure and evolution of stars that form carbon–oxygen (CO) white dwarfs. Paper F16 samples 26 reaction rates of the 405 total rates in the chosen reaction network, which can bias identifying the reactions that play a role in altering the stellar structure.

In this paper, we apply the same Monte Carlo framework to models of massive stars. We consider all forward reactions in a suitable reaction network (reverse rates are calculated by detailed balance) to eliminate potential biases from selecting a limited set of reactions. Our workflow couples temperature-dependent reaction rate uncertainties from STARLIB (Sallaska et al. 2013) with stellar models from Modules for Experiments in Stellar Astrophysics (MESA) (Paxton et al. 2011, 2013, 2015). We sample the reaction rates independently and simultaneously according to their respective PDFs. These sampled rates form input for $15M_{\odot}$ models evolved from the pre-main sequence to core O-depletion. We focus on $15M_{\odot}$ models because they approximately represent the most numerous SNe by number for a Salpeter initial mass function with slope $\Gamma = -1.35$, and a lower limit of $9M_{\odot}$ for stars that become SNe (Salpeter 1955; Scalo 1986; Sukhbold & Woosley 2014; Farmer et al. 2015). We consider solar and subsolar metallicities to explore the effect of reaction rate uncertainties on stars in different galactic environments.

This paper is novel in two ways. First, we sample a large number of reaction rates (665 forward reactions) in a Monte Carlo stellar model framework where the rates are sampled *before* the stellar model is evolved. This accounts for changes in the stellar structure due to reaction rate uncertainties, and is fundamentally different than post-processing schemes. Second, we quantify the variation of key quantities of the stellar models at five key evolutionary epochs. This allows determination of (1) the most important reactions overall, and (2) when these key reactions play a crucial role in the life of a massive star. In short, this paper presents the first Monte Carlo stellar evolution studies of massive stars that use PDFs for the nuclear reaction rate uncertainties and complete stellar models.

In Section 2 we describe the input physics of our models. In Section 3 we discuss our Monte Carlo stellar model framework and quantify the uncertainty of a few key nuclear reactions. Before presenting the results of our survey, we describe the characteristics of baseline $15M_{\odot}$ models evolved using *median* reaction rates from STARLIB in Section 4. In Section 5 we present our main results. In Section 6 we compare our results to previous efforts and make an assessment of the overall impact of the uncertainties due to nuclear reactions relative to other quantified sources of uncertainty (e.g., Farmer et al. 2016). We summarize our results in Section 7.

2. Input Physics

We evolve $15M_{\odot}$ models using MESA (version 7624, Paxton et al. 2011, 2013, 2015). All models begin with an initial metallicity of $Z = Z_{\odot} = 0.0153$ ("solar," Grevesse & Sauval 1998; Asplund et al. 2009; Caffau et al. 2010; Vagnozzi et al. 2017) or $Z = 2 \times 10^{-3} Z_{\odot} = 0.0003$ ("subsolar"). Solar metallicity models use isotopic distributions from Lodders et al. (2009), while subsolar models use the methods of West & Heger (2013).[7] The metallicity-dependent isotopic distributions from West & Heger (2013) reproduce α enhancement trends for a large sample of low-Z stars in the Milky Way halo (Frebel et al. 2010), thus motivating our choice for these distributions over solar-scaled compositions.

Farmer et al. (2016) show convergence of key quantities in $15M_{\odot}$ MESA models at the $\simeq$10% level when the reaction network contains $\gtrsim$127 isotopes. Following their results, each stellar model utilizes the in situ nuclear reaction network `mesa_127.net`, which follows 127 isotopes from ^{1}H to ^{64}Zn coupled by 1201 reactions. Figure 1 shows the 127 isotopes and their linking nuclear reactions. The isotopic abundance distributions we use contain 288 isotopes from ^{1}H to ^{238}U. We add the residual mass fraction ($\lesssim 10^{-5}$) of the 161 isotopes not

[7] Available from http://mesa-web.asu.edu/gce.html.

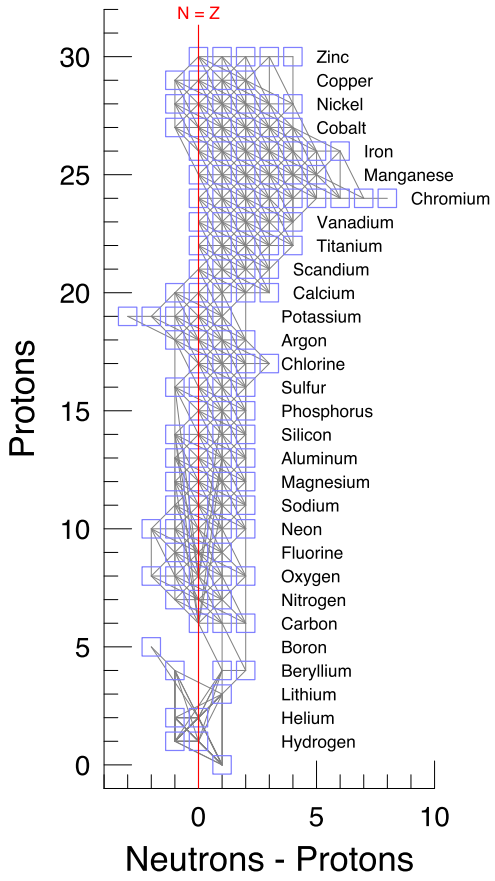

Figure 1. Proton number vs. neutron excess for the adopted 127 isotope reaction network. Thermonuclear and weak reaction rates coupling the isotopes are marked by gray lines, and symmetric matter ($N = Z$) is marked by a red line.

in the reaction network to the initial ^{1}H mass fraction to maintain baryon number conservation $\sum_{i=1}^{127} X_i = 1$, where X_i is the mass fraction of isotope i.

We include mass loss using the `Dutch` wind loss scheme (Nieuwenhuijzen & de Jager 1990; Nugis & Lamers 2000; Vink et al. 2001; Glebbeek et al. 2009) with an efficiency of $\eta = 0.8$. We neglect the effects of rotation, magnetic fields, and rotation-induced mass loss in this study.

We use the Ledoux criterion for convection with an efficiency parameter of $\alpha_{\rm MLT} = 2.0$, and the `mlt++` approximation for convection (Paxton et al. 2013). We include convective boundary mixing (overshoot, thermohaline, and semi-convection) with baseline values following Farmer et al. (2016). For convective overshoot we use $f = 0.004$ and $f_0 = 0.001$, which can reproduce mass entrainment rates found in idealized 3D simulations of explosive O-shell burning in massive stars (Jones et al. 2017). For simplicity, we apply the same overshoot efficiency to all boundaries. For thermohaline mixing, we use $\alpha_{\rm th} = 2.0$(Traxler et al. 2011; Brown et al. 2013; Garaud et al. 2015). Semi-convection uses an efficiency of $\alpha_{\rm sc} = 0.01$ (Spruit 2013; Zaussinger & Spruit 2013).

We use the MESA control `mesh_delta_coeff`, $\delta_{\rm mesh}$, to monitor mass resolution, which accounts for the gradients in the structure quantities to decide whether a cell should be split or merged. The default MESA value is unity. In this work, we use $\delta_{\rm mesh} = 0.5$. This results in ≃2300 cells at the terminal-age main sequence (TAMS), ≃4700 at core He-depletion, and ≃2100 cells during core O-burning. Section 4 discusses the sensitivity of our results to mass resolution.

We use several of MESA's timestep controls. The parameter `varcontrol_target`, $w_{\rm t}$, broadly controls the temporal resolution by restricting the allowed relative variation in the structure between timesteps. The default value is $w_{\rm t} = 1 \times 10^{-4}$. In this work, we use $w_{\rm t} = 5 \times 10^{-5}$, except during off-center C-burning where we use $w_{\rm t} = 1 \times 10^{-5}$ to further improve time resolution. We also control the rate of fuel depletion with the `delta_lg_X`* timestep controls, where the asterisk denotes a major fuel (i.e., H, He, C, Ne, or O). In total, we observe timesteps of $\Delta t \simeq 2 \times 10^4$ yr on the main sequence, $\Delta t \simeq 4 \times 10^3$ yr during core He-burning, and $\Delta t \simeq 12$ hr during core O-burning. Section 4 discusses the sensitivity of our results to temporal resolution.

For each stellar model, we sample 665 forward reaction rates from STARLIB Archived Version 5 (Sallaska et al. 2013) simultaneously and independently within their temperature-dependent uncertainties. We calculate reverse rates directly from the forward rates using detailed balance. We utilize the work of Alastuey & Jancovici (1978) and Itoh et al. (1979) for reaction rate screening factors. The fitting formula of Itoh et al. (1996) provides the thermal neutrino energy losses. Weak reactions rates, in order of precedence, are from Langanke & Martínez-Pinedo (2000), Oda et al. (1994), and Fuller et al. (1985).

Each stellar model evolves from the pre-main sequence until the central $X(^{16}{\rm O}) \simeq 1 \times 10^{-3}$. We use 1000 solar and subsolar stellar models, for a total of 2000 Monte Carlo stellar models. All MESA inlists and many of the stellar models are available at http://mesastar.org.

3. Reaction Rate Sampling

We construct a sampled nuclear reaction rate following Iliadis et al. (2015). We summarize the key characteristics here. The STARLIB rate library provides the *median* reaction rate, $\langle \sigma v \rangle_{\rm med}$, and the associated $f.u.$, over the temperature range 10^{6-10} K. A log-normal PDF is assumed for all reaction and decay rates, and these PDFs are described by the location and spread parameters, μ and σ, respectively. These parameters are obtained using the median rate and $f.u.$ tabulated in STARLIB as $\sigma = \ln f.u.$ and $\mu = \ln \langle \sigma v \rangle_{\rm med}$. These two parameters give a complete description of the probability density of the reaction rate at any temperature point and form the basis of our sampling scheme.

A sampled reaction rate is drawn from a log-normal distribution (e.g., Evans et al. 2000) for an arbitrary quantity, x, as

$$x_i = e^{\mu + \sigma p_i} \equiv e^{\mu} (e^{\sigma})^{p_i} . \quad (1)$$

Using the relations for μ and σ, we obtain a sampled rate distribution as a function of temperature from

$$\langle \sigma v \rangle_{\rm samp} = e^{\mu} (e^{\sigma})^{p_{i,j}} = \langle \sigma v \rangle_{\rm med} f.u.^{p_{i,j}}, \quad (2)$$

where $p_{i,j}$ is a standard Gaussian deviate with mean of zero and standard deviation of unity. The index i corresponds to the stellar model of grid size N and the index j corresponds to the number of reactions sampled.

We refer to $p_{i,j}$ as the rate variation factor for the jth reaction. From Equation (2), a rate variation factor of $p_{i,j} = 0$ corresponds to the *median* STARLIB reaction rate. For large

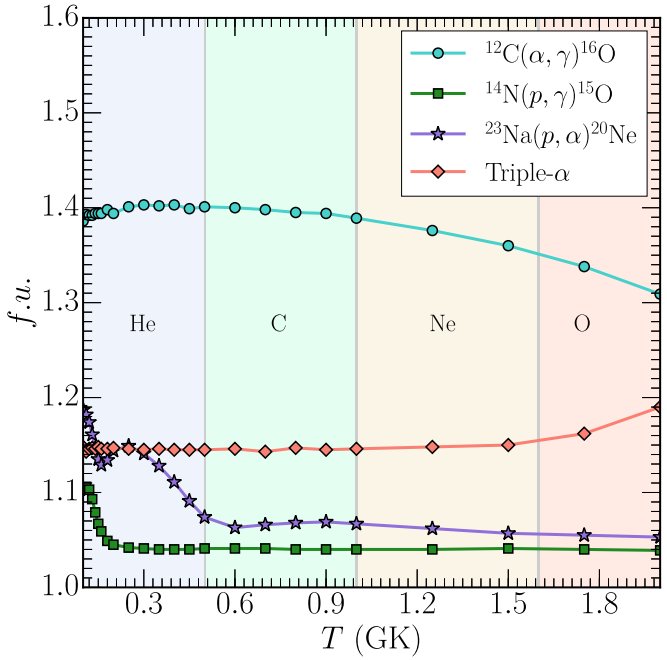

Figure 2. The factor uncertainty as a function of temperature provided by STARLIB for the $^{12}C(\alpha,\gamma)^{16}O$, $^{14}N(p,\gamma)^{15}O$, $^{23}Na(p,\ \alpha)^{20}Ne$, and triple-$\alpha$ reactions over different approximate core burning temperatures.

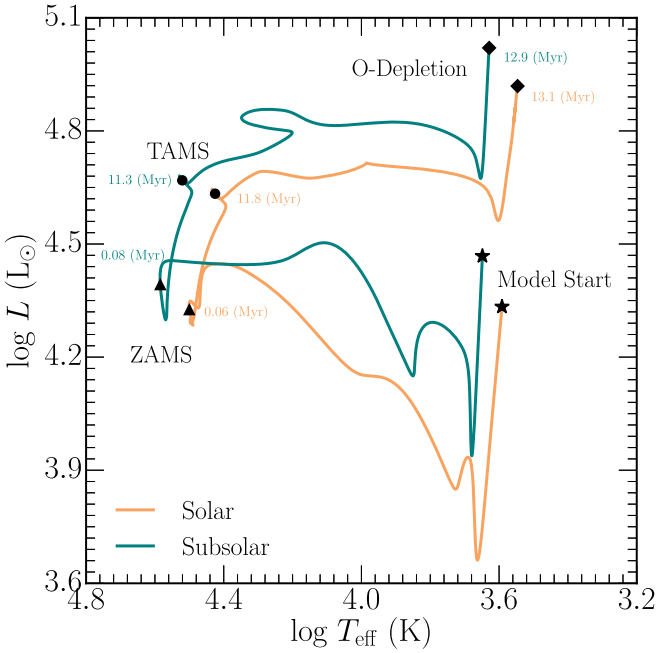

Figure 3. Hertzsprung–Russell diagram of the baseline $15M_\odot$ solar and subsolar models. Star symbols denote the beginning of each stellar model, triangles denote the ZAMS, circles denote the TAMS, and diamonds denote core O-depletion. Ages at these stages are annotated.

rate variation factors, the extent of change of the reaction rate at a given temperature point is limited by the factor uncertainty.

For example, for the $^{12}C(\alpha,\ \gamma)^{16}O$ reaction rate (Kunz et al. 2002), STARLIB shows that the largest value of factor uncertainty is $f.u. = 1.403$ at $T = 0.4$ GK. For typical extrema of a Gaussian distribution such as those used to generate our rate variation factors, one could expect values of $p_{i,j} = +3.5, -3.5$. In such a scenario, this would represent a change in the sampled nuclear reaction rate of $\langle\sigma v\rangle_{\rm samp} \simeq 3.27 \times \langle\sigma v\rangle_{\rm med}$ for $p_{i,j} = +3.5$ and $\simeq 0.31 \times \langle\sigma v\rangle_{\rm med}$ for $p_{i,j} = -3.5$ at $T = 0.4$ GK. At all other temperature points, the modification of the median rate may be less for the same value of $p_{i,j}$.

In Figure 2 we plot the $f.u.$ for the $^{12}C(\alpha,\gamma)^{16}O$, $^{14}N(p,\gamma)^{15}O$, $^{23}Na(p,\ \alpha)^{20}Ne$, and triple-$\alpha$ reaction rates over typical core He-, C-, Ne-, and O-burning temperatures. The $^{12}C(\alpha,\gamma)^{16}O$ rate has the largest factor uncertainty across the temperature ranges considered. At higher temperatures such as those expected in more advanced burning stages after core O-burning, the uncertainty in the $^{12}C(\alpha,\gamma)^{16}O$ rate begins to be overtaken by the uncertainty in the triple-α reaction.

We simultaneously and independently sample 665 forward thermonuclear reaction rates. For each reaction, we generate $N = 1000$ random Gaussian deviates to modify the reaction rates in the stellar models. Our choice for the sample size is motivated by the scaling of the sampling error for perfectly uncorrelated distributions. For such a distribution we expect a standard error of $\sigma/\sqrt{N} \simeq 3\%$. Since MESA calculates inverse rates directly from the forward rates using detailed balance, we also implicitly sample the corresponding 665 inverse rates. However, the corresponding inverse sampled rates are not independent of the forward sampled reactions.

Reaction rates derived from Monte Carlo sampling of experimental nuclear data are available for 33 of the 665 reactions considered (Iliadis et al. 2010, 2015, 2016; Sallaska et al. 2013). For other reactions, Monte Carlo or Bayesian derived rate distributions are not yet available. In these such cases, *median* rate values and the corresponding temperature-dependent $f.u.$ are obtained from estimates of experimental uncertainty where available. In the absence of experimental nuclear physics input, theoretical *median* reaction rates are obtained from Hauser–Feshbach model calculations with the TALYS software instrument (Goriely et al. 2008). Such theoretical rates are given a constant uncertainty of $f.u. = 10$ at all temperature points.

We assume that the random Gaussian deviate is independent of temperature, $p_{i,j}(T) =$ constant (Iliadis et al. 2015). This simplification yields similar levels of uncertainties to more intricate sampling schemes (Longland 2012). We stress that despite this simplification, the $f.u.$ provided by STARLIB is temperature-*dependent*. This allows us to follow changes in the uncertainty that may occur due to different resonance contributions.

The sampled reaction rate distributions are then constructed using Equation (2). Each nuclear reaction rate in STARLIB has a total of 60 T, $\langle\sigma v\rangle_{\rm med}$, and $f.u.$ data points. A sampled reaction rate also contains 60 data points and is then passed to MESA in tabular form. MESA interpolates between data points to construct a smoothed sampled nuclear reaction rate defined by 10,000 reaction rate data points as a function of T.

4. Properties of the Baseline $15M_\odot$ Stellar Models

Before presenting the results of our survey of Monte Carlo stellar models, we discuss the properties of the baseline $15M_\odot$ solar and subsolar models. These baseline models were evolved using the input physics described in Section 2 and the *median* STARLIB nuclear reaction rates. A *median* reaction rate is obtained in our sampling scheme by a Gaussian deviate of zero, $p_{i,j} = 0$.

Figure 3 shows a Hertzsprung–Russell diagram of the solar and subsolar baseline $15M_\odot$ stellar models. The start of the stellar models, the zero-age main sequence (ZAMS), terminal-age main sequence, and the ending point of core O-depletion are annotated. The subsolar model is brighter and hotter than the solar model primarily because a smaller metallicity decreases the opacity in the stellar atmosphere. At ZAMS, the subsolar model has a luminosity and effective temperature of $\log(L/L_\odot) \simeq 4.39$and $\log(T_{\rm eff}/{\rm K}) \simeq 4.58$while the solar model has $\log(L/L_\odot) \simeq 4.33$and $\log(T_{\rm eff}/{\rm K}) \simeq 4.50$. The solar model spends $\simeq$11.2 Myr on the main sequence while the subsolar model spends $\simeq$11.7 Myr.

The ZAMS homology relations for CNO burning, constant electron scattering opacity, and radiative transport (Hoyle & Lyttleton 1942; Faulkner 1967; Pagel & Portinari 1998; Bromm et al. 2001; Portinari et al. 2010) are

$$\begin{aligned}\frac{T_{\rm eff}}{3\times10^4\ {\rm K}} &\simeq \left(\frac{Z}{Z_\odot}\right)^{-1/20}\left(\frac{M}{15M_\odot}\right)^{1/40}\\ \frac{R}{6R_\odot} &\simeq \left(\frac{Z}{Z_\odot}\right)^{1/11}\left(\frac{M}{15M_\odot}\right)^{5/11}\\ \frac{L}{2\times10^4L_\odot} &\simeq \left(\frac{Z}{Z_\odot}\right)^{-1/55}\left(\frac{M}{15\,M_\odot}\right).\end{aligned} \quad (3)$$

The ZAMS positions of the solar and subsolar models in Figure 3 are commensurate with the trends of Equation (3).

At the TAMS, the nascent He-rich core is surrounded by a thin H-burning shell. The core contracts and its temperature increases, while the outer layers of the star expand and cool. The star becomes a red giant (e.g., Iben 1966, 1991; Stancliffe et al. 2009; Karakas & Lattanzio 2014). The solar model spends $\simeq$1.54 Myr undergoing convective core He-burning and the subsolar model spends $\simeq$1.27 Myr. At He-depletion, the solar model has a He-core mass of $M_{\rm He\text{-}Core} \simeq 4.24\,M_\odot$ and a $^{12}{\rm C}/^{16}{\rm O}$ ratio of 0.34. The subsolar model has a more massive, slightly more C-rich core with $M_{\rm He\text{-}Core} \simeq 4.80\,M_\odot$ and $^{12}{\rm C}/^{16}{\rm O} \simeq 0.36$.

The trajectory of the baseline models in the T–ρ plane is shown in Figure 4. In general, the tracks are qualitatively similar. The largest difference is that the subsolar model undergoes hotter, less dense core burning. This is a result of the decreased stellar envelope opacity and larger luminosity shown in Figure 3. Figure 5 shows Kippenhahn diagrams for the baseline models after core He-burning. The C-burning features of both baseline models are similar; they both ignite carbon convectively at the core and undergo three convective C-burning flashes that recede outward in mass coordinate.

After C-depletion, the photodisintegration of ^{20}Ne drives convective core Ne-burning. This burning phase lasts $\simeq$1.7 yr for the solar model and $\simeq$0.33 yr for the subsolar model. After Ne-depletion, core O-burning begins at $T_{\rm c} \simeq 1.8\times10^9$ K and $\rho_{\rm c} \simeq 9.1\times10^6\,{\rm g\,cm^{-3}}$. The initial core O-burning episode is energetic enough to drive a large convection region that initially extends to $\simeq 0.9\,M_\odot$. At core O-depletion, we find a composition of $X_{\rm c}(^{32}{\rm S}) \simeq 0.524$, $X_{\rm c}(^{34}{\rm S}) \simeq 0.189$, and $X_{\rm c}(^{28}{\rm Si}) \simeq 0.244$ for the solar model. Other isotopes show central mass fractions of $X_{\rm c} \lesssim 10^{-2}$. The subsolar model has an O-depletion composition of $X_{\rm c}(^{32}{\rm S}) \simeq 0.522$, $X_{\rm c}(^{34}{\rm S}) \simeq 0.175$, and $X_{\rm c}(^{28}{\rm Si}) \simeq 0.236$ with other burning products having negligible central mass fractions. The central electron fraction at this point is $Y_{\rm e,c} \simeq 0.4936$ and $Y_{\rm e,c} \simeq 0.4942$ for the solar and subsolar models, respectively. Our choice of stopping criterion does not signify the end of O-burning.

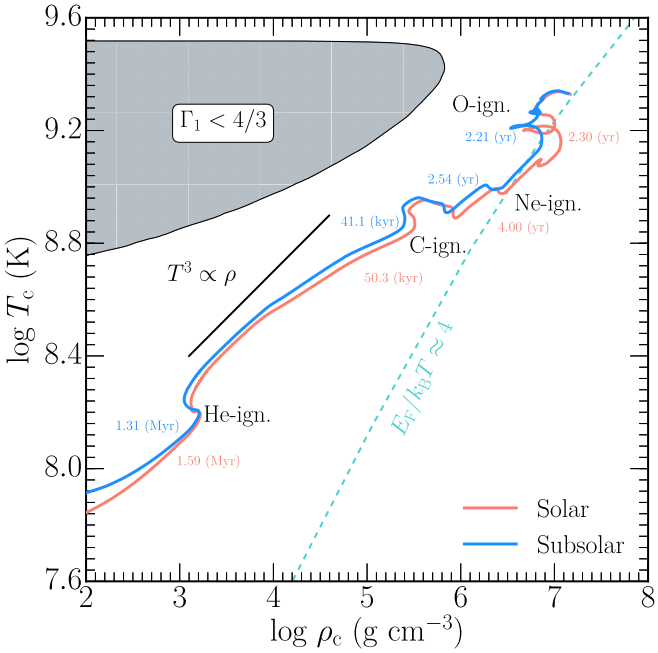

Figure 4. Evolution of the central density and temperature for the solar and subsolar baseline models. Approximate core-burning locations, times until O-depletion, radiation entropy scaling relation—$T^3 \propto \rho$, electron degeneracy line $E_{\rm F}/k_{\rm B}T \simeq 4$ where $E_{\rm F}$ is the Fermi energy, and electron–positron pair-dominated region are annotated.

Lastly, we consider the impact of mass and temporal resolution on key physical parameters relevant to this paper by evolving eight additional baseline models. Figure 6 shows the results for $\delta_{\rm mesh} = (1.0, 0.25)$at our fixed baseline temporal resolution of $w_{\rm t} = 5\times10^{-5}$, and for $w_{\rm t} = (5\times10^{-4}, 1\times10^{-5})$ at our baseline mass resolution of $\delta_{\rm mesh} = 0.5$. Otherwise the solar and subsolar models use the same *median* reaction rates and input physics as the baseline models. For $\delta_{\rm mesh}$, the largest variation is $\simeq$13% in the central density for the subsolar models. All other quantities have variations $\lesssim$7% at the highest mass resolution considered. For $w_{\rm t}$, the largest variation is $\lesssim$5% in the central density, and all other quantities have variations of $\lesssim$3%.

5. Monte Carlo Stellar Models

We evolve two grids of Monte Carlo stellar models. The first grid consists of 1000 Monte Carlo stellar models at solar metallicity. Each model has a different set of sampled nuclear reactions; otherwise each model has the same input physics as the baseline model. We refer to this set of models as the "solar grid." The second set consists of 1000 models at a metallicity of $Z = 0.0003$, henceforth the "subsolar grid." Each stellar model takes $\simeq$60 hr on four CPUs. The total computational expense is $\simeq$0.48 M CPU hours and it generates $\simeq$1 TB of data.

Some properties of a stellar model may be more important at different evolutionary phases. For example, the time spent on the main sequence is a direct consequence of the $^{14}{\rm N(p,\gamma)^{15}O}$ reaction, which modulates the rate at which the CNO cycle may proceed (Imbriani et al. 2004). At core He-depletion, the central carbon mass fraction, temperature, or density affects whether carbon ignites radiatively or convectively (Lamb et al. 1976;

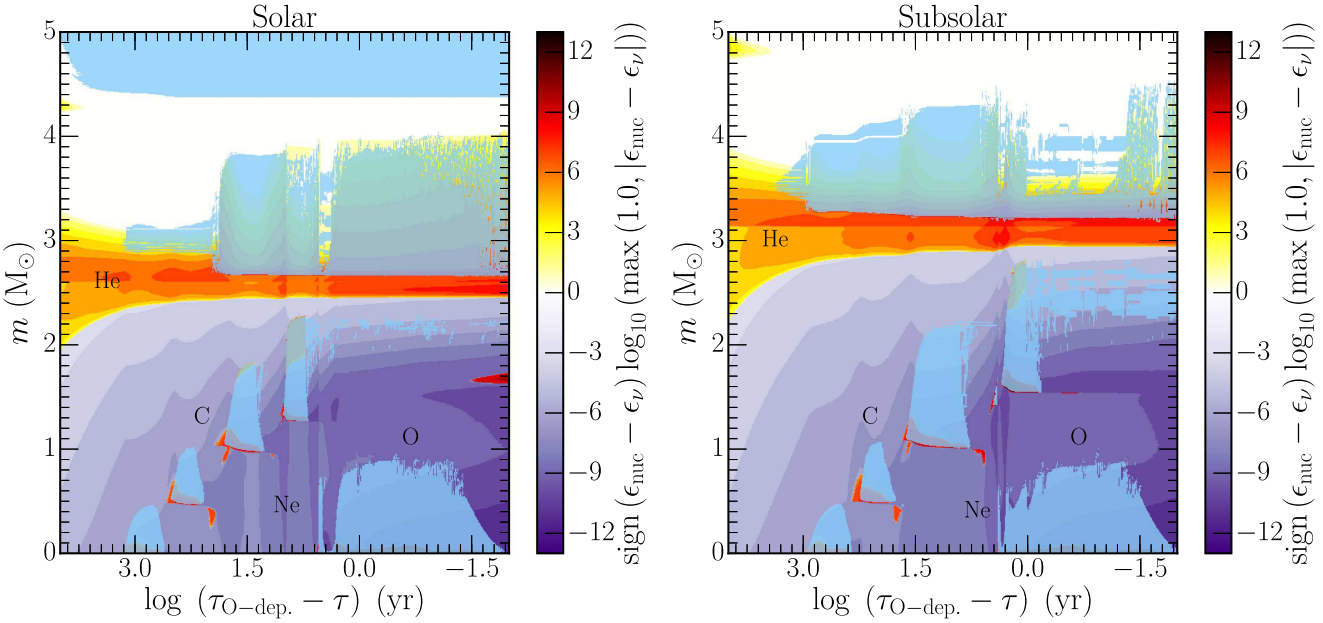

Figure 5. Kippenhahn diagrams for the solar (left) and subsolar (right) baseline stellar models after core He-burning. Annotated are the He-burning shell and the convective C-, Ne-, and O-burning episodes. The x-axis is the logarithmic difference between the age at O-depletion, $\tau_{\rm O\text{-}dep.}$, and the current age of the model, τ. Dark orange to red correspond to regions of strong nuclear burning, light to dark purple to cooling regions, and white to regions balancing heating and cooling. Blue shows convective regions, gray marks regions of convective overshoot. Semi-convective and thermohaline regions are not shown.

Woosley & Weaver 1986; I. Petermann et al. 2017, in preparation). Such features are directly linked to key nuclear reaction rates. We thus consider different properties of our stellar models at five evolutionary epochs: central H-, He-, C-, Ne-, and O-depletion. The properties considered at each epoch are commonly held to be significant for connecting pre-supernova stellar models to observed transients, for stellar yields for chemical evolution, or for predicting SN properties (e.g., Nomoto et al. 2013; Couch et al. 2015; Janka et al. 2016; Côté et al. 2017).

To determine the reaction rates that have the largest impact on different properties of the stellar models at different evolutionary phases, we use a Spearman rank-order correlation (SROC) analysis. An SROC is the Pearson correlation coefficient between the rank values of two variables (Myers & Well 1995). The N raw scores A_i and B_i are converted to ranks rgA_i and rgB_i, sorted in descending order according to magnitude, and the SROC is

$$r_{\rm s} = \frac{{\rm cov}({\rm rg}A, {\rm rg}B)}{\sigma_{{\rm rg}A}\,\sigma_{{\rm rg}B}}\,, \tag{4}$$

where cov(rg$A$, rg$B$) is the covariance matrix of the two variables A_i and B_i, and $\sigma_{{\rm rg}A}$ and $\sigma_{{\rm rg}B}$ are the standard deviations of A and B, respectively. An SROC of $r_{\rm s} = +1$ represents a perfectly monotonically increasing relationship, $r_{\rm s} = 0$, perfectly uncorrelated, and $r_{\rm s} = -1$, monotonically decreasing.

5.1. Hydrogen Depletion

We consider six properties at core H-depletion, which we define as the time point when the central ^{1}H mass fraction drops below $\simeq 10^{-6}$: the mass of the He core $M_{\rm He\text{-}Core}$, age $\tau_{\rm TAMS}$, central temperature $T_{\rm c}$, central density $\rho_{\rm c}$, compactness parameter—effectively the depth of the gravitational potential well at the expected maximum mass of a neutron star —$\xi_{2.5} = M/R|_{m=2.5\,M_\odot}$, and central ^{14}N mass fraction $X_{\rm c}(^{14}{\rm N})$.

5.1.1. Probability Distribution Functions

Figure 7 shows the PDFs of these six properties of the stellar models at this epoch. The x-axis is the variation, $(X_i - \bar{X})/\bar{X}$, where X_i is a value of a property for a single model and $\bar{X}$ is the arithmetic mean of the distribution. The amplitude of the histogram corresponds to the fraction of the 1000 models within a given bin. In this paper, the number of bins is chosen according to the Rice rule, $k = 2n^{1/3}$, where k is the number of bins and n is the number of samples (Lane 2013). While different bin widths can reveal different features of the distribution, we find this choice of bins sufficient for the discussion of the histograms presented here.

Throughout this paper we use the 95% confidence interval (CI) limits. These are defined, for each PDF, to be the limits corresponding to the unique cumulative distribution function containing 95% of the PDF. This allows reporting of the most likely ($\sim 2\sigma$) values of a property without the effects of outliers in the data. This definition is different than a canonical CI derived from an assumed distribution function model of the data.

We define $M_{\rm He\text{-}Core}$ as the mass coordinate where $X(^1{\rm H}) < 0.01$ and $X(^4{\rm He}) > 0.1$. The 95% CI widths of the $M_{\rm He\text{-}Core}$ PDFs span a narrow $\simeq \pm 0.1\%$ across the mean of the distribution for both solar and subsolar models. Both PDFs show well-defined zero-variation peaks of 2.80 $M_\odot$ for the solar models and 2.86 $M_\odot$ for the subsolar models.

The 95% CI width of the $\tau_{\rm TAMS}$ PDF for the solar models, $\simeq \pm 0.2\%$, is larger than the width of the PDF for the subsolar models, $\simeq \pm 0.1\%$. We defer an explanation of this difference until we discuss Figure 8. The solar and subsolar PDFs are symmetric about their zero-variation values of 11.3 Myr and 11.8 Myr, respectively.

The $T_{\rm c}$ and $\rho_{\rm c}$ PDFs show that the solar models are slightly cooler and less dense than the subsolar models, with zero-variation values of $T_{\rm c} \simeq (62.8\,{\rm MK}, 80.7\,{\rm MK})$ and $\rho_{\rm c} \simeq (42.4\,{\rm g\,cm^{-3}}, 88.2\,{\rm g\,cm^{-3}})$, respectively. After H-depletion,

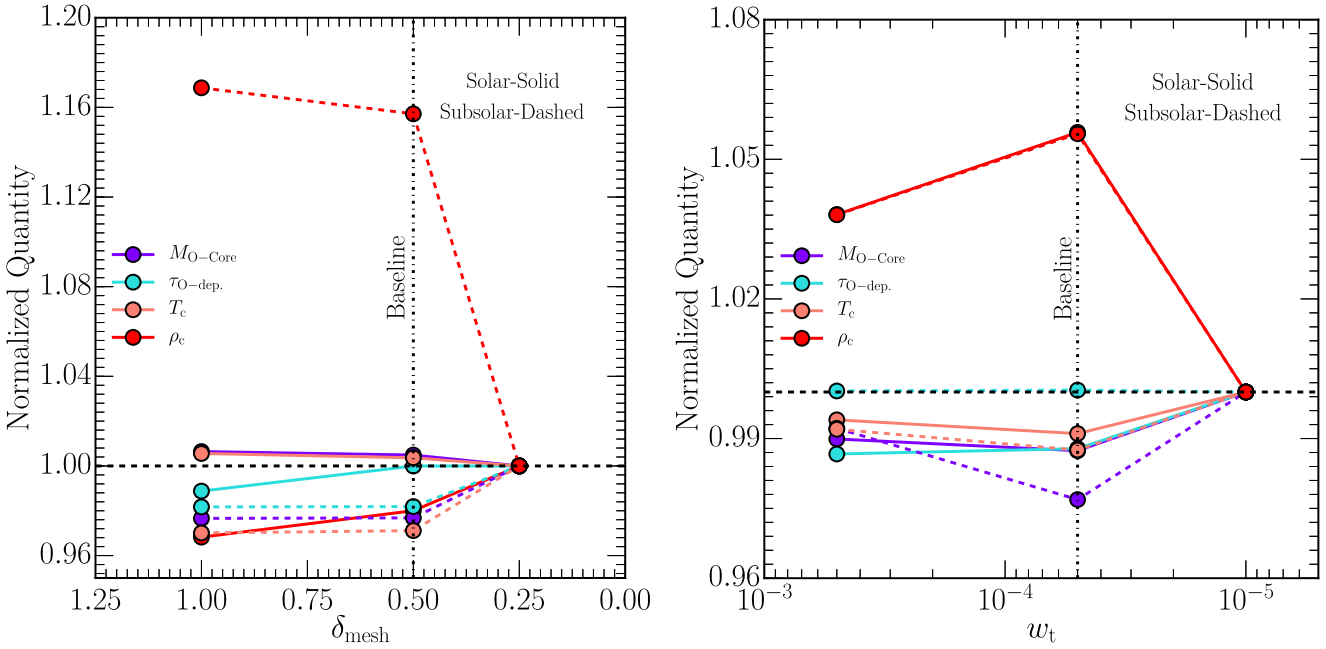

Figure 6. Four normalized quantities at core O-depletion as a function of the mass (left) and temporal (right) resolution controls $\delta_{\rm mesh}$ and $w_{\rm t}$: mass of the oxygen core —$M_{\rm ONe\text{-}Core}$, age—$\tau_{\rm O\text{-}dep.}$, central temperature—$T_{\rm c}$, and central density—$\rho_{\rm c}$. All quantities are normalized to their values at $\delta_{\rm mesh} = 0.25$ and $w_{\rm t} = 1 \times 10^{-5}$. A vertical black dashed–dotted line marks the resolution used for the Monte Carlo stellar models. A black dashed horizontal line marks a value of unity, i.e., no variance with respect to changes in mass or temporal resolution. Solid lines correspond to the solar models and dashed lines to the subsolar models.

the solar models will proceed to burn He at a cooler core temperature but in a denser core. This trend is seen in Figure 4. Note that the subsolar models have larger $T_{\rm c}$ and yet *longer* lifetimes $\tau_{\rm TAMS}$. In addition, the 95% CI widths of the $T_{\rm c}$ PDFs are $\simeq$1.2%, and the 95% CI widths of the $\rho_{\rm c}$ PDFs are $\simeq$4%.

Traditionally $\xi_{2.5}$ is evaluated at core-collapse. Our motivation for measuring $\xi_{2.5}$ starting at H-depletion is to assess the evolution of the variability in $\xi_{2.5}$; when do significant variations first arise and how do the variations grow? The 95% width of the $\xi_{2.5}$ PDF at H-depletion, $\simeq$1.2%, is dependent upon the narrow $M_{\rm He\text{-}Core}$ PDF and the wider $\rho_{\rm c}$ PDF. In addition, $\xi_{2.5}$ depends on the gradient of the density profile. The zero-variation values of the solar and subsolar grids show small differences at this epoch with $\xi_{2.5} \simeq (7 \times 10^{-3}, 8 \times 10^{-3})$, respectively.

Nitrogen is the dominant metal in the ashes of H-burning in massive stars because the ^{14}N(p, γ)^{15}O rate is the lowest in the CNO cycles (e.g., Iben 1966). This is reflected in the $X_{\rm c}(^{14}{\rm N})$ PDFs by the zero-variation values, 9.2×10^{-3} for the solar models and 1.9×10^{-4} for the subsolar models, being approximately equal to the sum of the ZAMS CNO mass fractions. The 95% CI width of the $X_{\rm c}(^{14}{\rm N})$ PDF, $\simeq \pm 1\%$, is consistent with the spreads in the other quantities measured.

5.1.2. Spearman Correlation Coefficients

Figure 8 shows the SROC coefficients for the solar and subsolar grids. The coefficients for the solar grid are shown by circles and those for the subsolar grid by diamond markers. A positive correlation coefficient is represented by a blue marker and a negative one by a red marker. For each property shown, the rate identifier corresponding to the SROC coefficients with the largest magnitude is marked by a vertical dashed line and label.

The ^{14}N(p, γ)^{15}O rate has a large impact on all the quantities we measure. For example, this rate has the largest SROC coefficient for $\tau_{\rm TAMS}$, with $r_{\rm s} \simeq +0.99$ for the solar and subsolar models. Coefficients of the remaining 664 reactions are significantly smaller, $\mathcal{O}(10^{-2})$. This suggests that $\tau_{\rm TAMS}$ is directly dependent on the ^{14}N(p, γ)^{15}O rate, with a larger rate *increasing* the lifetime to core H-depletion (e.g., Imbriani et al. 2004; Weiss et al. 2005; Herwig et al. 2006).

Increasing a reaction rate usually increases the generation rate of nuclear energy, which is deposited into thermal energy. The core temperature rises. Via the equation of state, the pressure increases, which causes the stellar core to expand. This expansion decreases $T_{\rm c}$ and $\rho_{\rm c}$, and thus causes nuclear burning to proceed at a slower rate. The net result of increasing an energetically important reaction rate is a longer burning lifetime and a decreased $T_{\rm c}$ and $\rho_{\rm c}$. This is the well-known thermostat mechanism (e.g., Hansen et al. 2004; Iliadis 2007).

Figure 9 shows the age and $T_{\rm c}$ at H-depletion for the solar models as a function of the rate multiplier applied at maximum *f.u.* for the ^{14}N(p, γ)^{15}O reaction. Least-squares fits to the linear trends yield the slope of the thermostat mechanism: $d\tau_{\rm TAMS}/dT_{\rm c}$, $\simeq -0.03$ Myr MK^{-1}. This correlation is confirmed by the large and negative SROC coefficients between the ^{14}N(p, γ)^{15}O rate and $\xi_{2.5}$, $T_{\rm c}$, and $\rho_{\rm c}$. The thermostat mechanism also causes the slightly larger zero variation of $M_{\rm He\text{-}Core}$ for the subsolar models relative to the solar models in Figure 7.

5.1.3. Impact of the Measurement Point

To assess the impact of the choice of measurement point, we repeat our SROC analysis during core H-burning at the point $X_{\rm c}(^{1}{\rm H}) \simeq X_{\rm c}(^{4}{\rm He})$. We compare the magnitude of the SROC values for $\tau_{\rm TAMS}$, $T_{\rm c}$, $\rho_{\rm c}$, and $\xi_{2.5}$ for both the solar and subsolar models.

Qualitatively, ^{14}N(p, γ)^{15}O still drives the variation in the age with a positive correlation, and the variations in $T_{\rm c}$, $\rho_{\rm c}$, and $\xi_{2.5}$ with negative correlations. The difference in the SROC values between the two epochs agrees to $\lesssim$0.01 for $T_{\rm c}$, $\rho_{\rm c}$, and

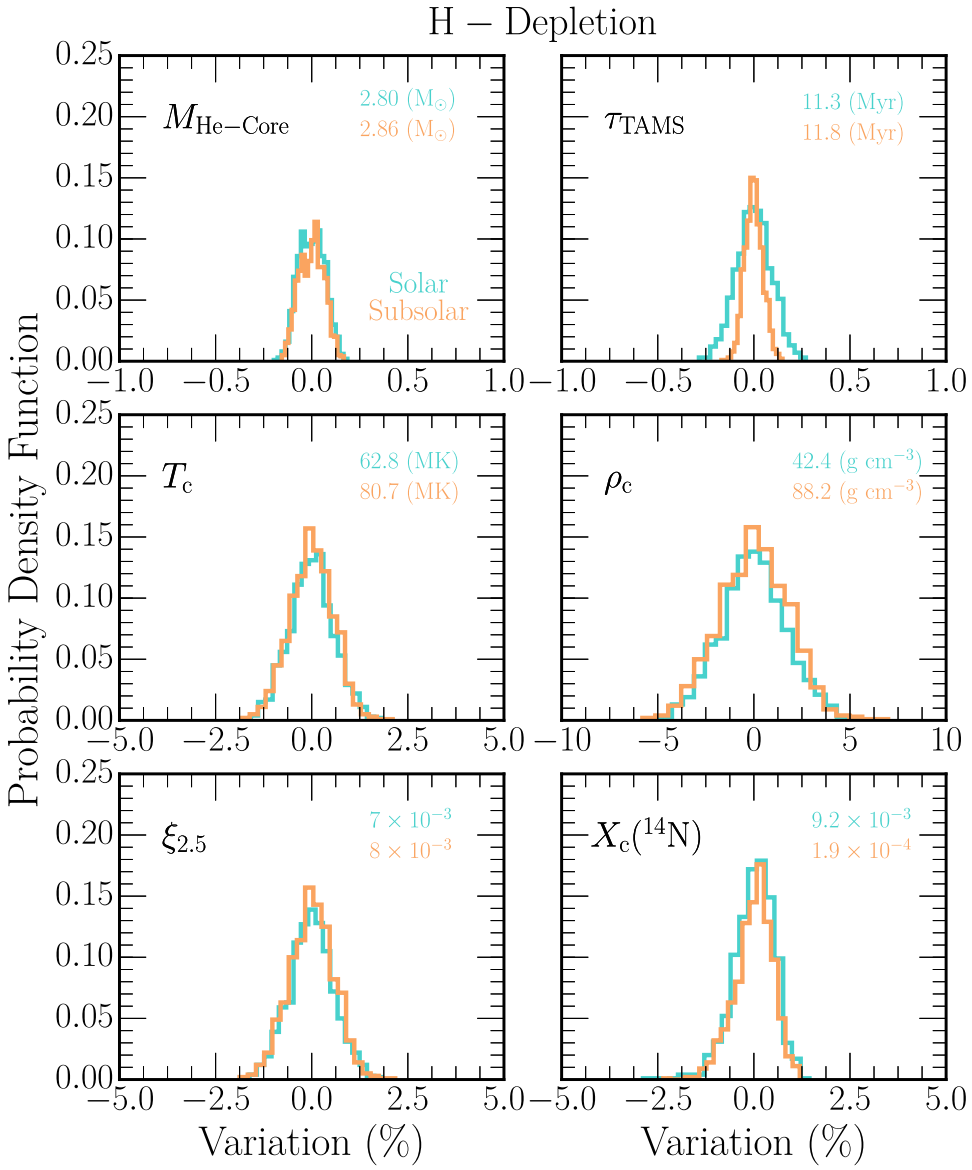

Figure 7. Probability density functions for six properties of the grid of Monte Carlo stellar models. The x-axis represents the difference between a model value for a given property and the arithmetic mean of all values obtained for that property. This quantity is then normalized to the mean of the distribution. This distribution is referred to as the "variation." The blue histograms correspond to the solar models while the tan histograms denote the subsolar models. The properties shown are $M_{\rm He\text{-}Core}$—the mass of the He core, $\tau_{\rm TAMS}$—the age at hydrogen depletion, $T_{\rm c}$—central temperature, $\rho_{\rm c}$—central density, $\xi_{2.5}$—compactness parameter measured at $m = 2.5\,M_\odot$, and $X_{\rm c}(^{14}{\rm N})$—central ^{14}N mass fraction. All properties are measured at H-depletion, when $X(^1{\rm H}) \lesssim 10^{-6}$. Annotated are the arithmetic means of each property corresponding to a variation of zero.

$\xi_{2.5}$ and to $\lesssim$0.2 for $\tau_{\rm TAMS}$. This re-evaluation suggests that the PDFs vary slightly based on the chosen measurement point and that identifying the key reactions from the SROC analysis is an invariant.

5.2. Helium Depletion

We measure the integrated impact of the uncertainties in the reaction rates at the point when the central helium mass fraction $X(^4{\rm He}) \lesssim 10^{-6}$.

5.2.1. Probability Distribution Functions

Figure 10 shows the PDFs of eight properties from the stellar models at this epoch: mass of the CO core $M_{\rm CO\text{-}Core}$, the elapsed time between H-depletion and He-depletion $\tau_{\rm He\text{-}burn}$, central temperature $T_{\rm c}$, central density $\rho_{\rm c}$, central ^{22}Ne mass fraction $X_{\rm c}(^{22}{\rm Ne})$, compactness parameter $\xi_{2.5}$, central ^{12}C mass fraction $X_{\rm c}(^{12}{\rm C})$, and central ^{16}O mass fraction $X_{\rm c}(^{16}{\rm O})$.

The 95% CI width of the $M_{\rm CO\text{-}Core}$ PDF spans $\simeq \pm 2\%$ for the solar and subsolar grids. Both PDFs show a well-defined peak of 2.41 $M_\odot$ for the solar models and 2.95 $M_\odot$ for the subsolar models and an extended tail for negative variations. That is, changes in the reaction rates are more likely to produce smaller C cores than more massive C cores. This asymmetry accounts for the PDFs not being centered at zero variation.

The solar and subsolar grid PDFs for $\tau_{\rm He\text{-}burn}$ have a 95% CI spread of $\simeq \pm 1\%$, suggesting that rate uncertainties have a smaller impact on $\tau_{\rm He\text{-}burn}$. The solar PDF is slightly wider than the subsolar PDF, and both PDFs are symmetric about their respective arithmetic means.

The $T_{\rm c}$ and $\rho_{\rm c}$ PDFs show 95% CI widths of $\simeq \pm 1.5\%$ and $\simeq \pm 3.5\%$, respectively, for both solar and subsolar models.

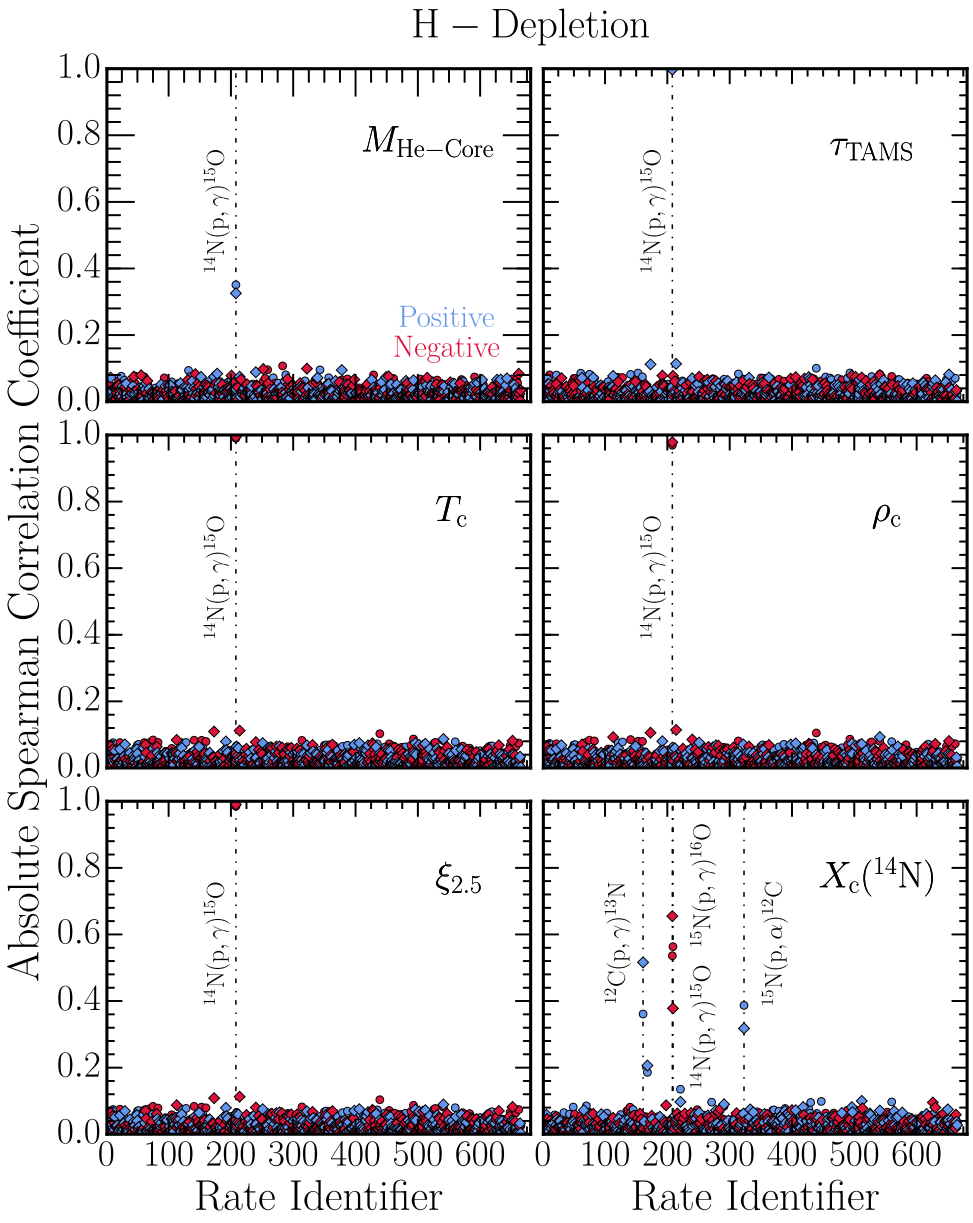

Figure 8. The absolute Spearman rank-order correlation coefficients for the 665 independently sampled thermonuclear reaction rates for the solar and subsolar grid of 1000 Monte Carlo stellar models. For a single nuclear reaction, the array of 1000 Gaussian deviates that were used to construct the sampled rate distributions is compared to six properties of the stellar models to determine the correlation coefficient. The solar metallicity coefficients are denoted by circles and subsolar metallicity by diamonds. A positive correlation is denoted by a blue marker while a negative coefficient is represented by a red marker. The *x*-axis corresponds to an arbitrary "rate identifier" used to track the thermonuclear reaction rates sampled in this work. The quantities considered are $M_{\rm He\text{-}Core}$—the mass of the He core, $\tau_{\rm TAMS}$—the age, $T_{\rm c}$—the central temperature, $\rho_{\rm c}$—the central density, $\xi_{2.5}$—the compactness parameter, and $X_{\rm c}(^{14}{\rm N})$—the central nitrogen-14 mass fraction. All quantities are measured when $X_{\rm c}(^{1}{\rm H}) \lesssim 1 \times 10^{-6}$. Key nuclear reactions with large SROC values are annotated.

Both PDFs are centrally peaked with $\lesssim$1% differences between the arithmetic means of the solar and subsolar models. Both PDFs exhibit long tails in the direction of positive variation, indicating that some combinations of the reaction rates produce cores that are $\simeq$5% hotter than the mean and $\simeq$10% denser than the mean.

The solar and subsolar grid PDFs for $X_{\rm c}(^{22}{\rm Ne})$ are nearly the same. However, the arithmetic means of the two PDFs differ by a factor of $\simeq$50. The reason for this difference is that most of a ZAMS star's initial metallicity Z comes from the CNO and ^{56}Fe nuclei inherited from its ambient interstellar medium. The slowest step in the hydrogen-burning CNO cycle is $^{14}{\rm N}({\rm p},\gamma)^{15}{\rm O}$, which causes all the CNO catalysts to pile up at ^{14}N at core H-depletion. During He-burning the sequence $^{14}{\rm N}(\alpha,\gamma)^{18}{\rm F}(\beta^{+},\nu_e)^{18}{\rm O}(\alpha,\gamma)^{22}{\rm Ne}$ converts all of the ^{14}N into the neutron-rich isotope ^{22}Ne. Thus, $X_{\rm c}(^{22}{\rm Ne})$ at core He-depletion is linearly dependent on the initial CNO abundances. The subsolar models have $\simeq$50 times less initial CNO than the solar models, accounting for the difference in the arithmetic means.

The solar and subsolar PDFs for $\xi_{2.5}$ are similar in peak amplitude, 95% CI width ($\simeq$1.2%), symmetry about zero variation, and mean arithmetic value. That is, rate uncertainties have little impact on differentiating between solar and subsolar metallicities. Similar to the $T_{\rm c}$ and $\rho_{\rm c}$ PDFs, there are outlier models whose combinations of reaction rates produce larger $\xi_{2.5}$.

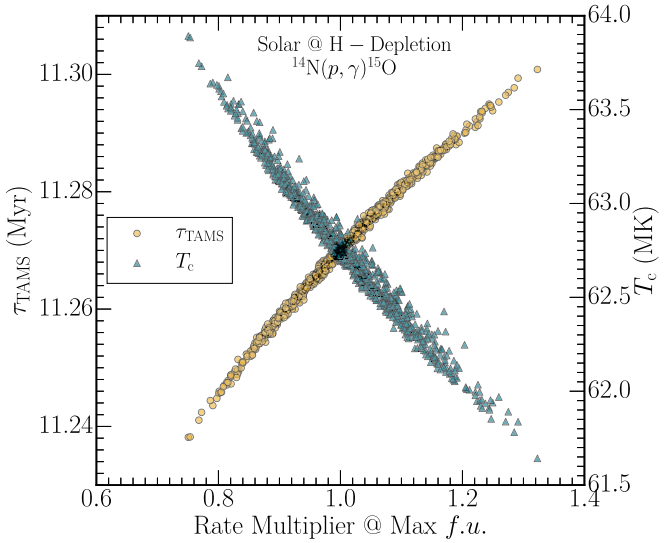

Figure 9. The age and central temperature at H-depletion as a function of the maximum rate multiplier applied to the ^{14}N(p, γ)^{15}O reaction rate for the grid of solar metallicity stellar models. The maximum $f.u.$ for ^{14}N(p, γ)^{15}O is $\simeq$1.1. Best-fit lines to the two trends yield the slope of the thermostat mechanism to be $d\tau_{\rm TAMS}/dT_{\rm c} \simeq -0.03$ Myr MK^{-1}.

The largest variations occur in the $X_{\rm c}(^{12}{\rm C})$ and $X_{\rm c}(^{16}{\rm O})$ PDFs with 95% CI widths of $\simeq \pm 70\%$ and $\simeq \pm 25\%$, respectively. The common driver for these variations are the triple-α, ^{12}C(α, γ)^{16}O, and ^{16}O(α, γ)^{20}Ne rates, whose roles we discuss below.

5.2.2. Spearman Correlation Coefficients

Figure 11 shows the SROCs for the 665 independently sampled thermonuclear reaction rates against the eight quantities considered in Figure 10. $M_{\rm CO\text{-}Core}$ is chiefly set by the ^{12}C(α, γ)^{16}O rate with $r_{\rm s} \simeq +0.8$ for both metallicity grids. Larger ^{12}C(α, γ)^{16}O rates build larger CO core masses. The triple-α rate plays a smaller role with $r_{\rm s} \simeq -0.17$ for both metallicity grids. Similarly, $\tau_{\rm He\text{-}burn}$ is primarily set by the ^{12}C(α, γ)^{16}O rate with coefficients of $r_{\rm s} = (+0.92, +0.94)$, respectively. The triple-α rate plays a less significant role with $r_{\rm s} \simeq -0.25$.

In contrast, $T_{\rm c}$ and $\rho_{\rm c}$ are chiefly affected by the uncertainties in the triple-α rate with $r_{\rm s} \simeq -0.8$ and $r_{\rm s} \simeq -0.7$, respectively. These large negative SROCs mean that the thermostat mechanism, discussed for H-burning—i.e., that reaction rates producing greater energy yield cooler and less dense cores—operates during He-burning. The ^{12}C(α, γ)^{16}O and ^{16}O(α, γ)^{20}Ne rates play smaller roles with $r_{\rm s} \leqslant +0.4$. Note that the positive correlation means larger ^{12}C(α, γ)^{16}O rates produce hotter cores, in juxtaposition to the triple-α rate. This is because a larger ^{12}C(α, γ)^{16}O rate converts more carbon into oxygen, so the core burns hotter at any given triple-α rate (which dominates the energy generation) to satisfy the luminosity demanded by the surface of the stellar model. Outliers with positive variations in the $T_{\rm c}$ and $\rho_{\rm c}$ PDFs of Figure 10 are caused by combinations of the ^{12}C(α, γ)^{16}O and triple-α reactions. For a small triple-α rate, the model will be hotter and denser. When this is coupled with a large ^{12}C(α, γ)^{16}O rate, the stellar models at He-depletion have a hotter and denser core with $T_{\rm c}$ increased by $\simeq$+5% and $\rho_{\rm c}$ increased by $\simeq$+10%.

The mass fraction of the neutron-rich ^{22}Ne isotope is set by the competition between the triple-α and ^{22}Ne(α,γ)^{26}Mg rates. The triple-α rate sets $T_{\rm c}$ and $\rho_{\rm c}$, with a larger rate giving cooler and denser cores that favor the production of ^{22}Ne by the sequence ^{14}N(α,γ)^{18}F(β^+, ν_e)^{18}O(α,γ)^{22}Ne. This is the origin of the positive SROC coefficient for the triple-α rate in the solar and subsolar grids. On the other hand, ^{22}Ne(α,γ)^{26}Mg destroys ^{22}Ne, storing the neutron excess in ^{26}Mg. This accounts for the negative SROC coefficient of ^{22}Ne(α,γ)^{26}Mg for both metallicity grids.

$\xi_{2.5}$ is chiefly set by the triple-α rate with $r_{\rm s} = -0.83$ and $r_{\rm s} = -0.74$ for the solar and subsolar models respectively. A larger triple-α rate produces a smaller $\xi_{2.5}$, due to the decrease in overall density of the stellar core. For the subsolar models the ^{16}O(α, γ)^{20}Ne rate plays a smaller role ($r_{\rm s} = -0.34$), but also decreases $\xi_{2.5}$ as the rate becomes larger. The solar and subsolar PDFs for $\xi_{2.5}$ show outliers with variations up to $\simeq$5%. These outliers form from the same combination of reaction rates that produces denser stellar models. That is, models with high $\xi_{2.5}$ have either a depressed triple-α rate, an enhanced ^{12}C(α, γ)^{16}O rate, or both.

During quiescent He-burning the triple-α process and the ^{12}C(α, γ)^{16}O reaction burn with high efficiency through pronounced resonance mechanisms (e.g., deBoer et al. 2017). In contrast, the ^{16}O(α, γ)^{20}Ne reaction lacks any such resonance enhancement in the stellar energy range, making its rate comparatively much lower. This essentially prohibits significant He-burning beyond ^{16}O and maintains the ^{12}C/^{16}O balance we observe today.

The ^{12}C(α, γ)^{16}O rate sets $X_{\rm c}(^{12}{\rm C})$ and $X_{\rm c}(^{16}{\rm O})$ for both solar and subsolar models with $r_{\rm s} \simeq -0.95$ and $r_{\rm s} \simeq +0.95$, respectively. A larger ^{12}C(α, γ)^{16}O rate destroys more C and produces more O. The triple-α rate plays a smaller role in setting $X_{\rm c}(^{12}{\rm C})$ and $X_{\rm c}(^{16}{\rm O})$ with $r_{\rm s} \simeq +0.29$ and $r_{\rm s} \simeq -0.28$, respectively. A larger triple-α rate produces more C and less O. These results suggest that $X_{\rm c}(^{12}{\rm C})$ and $X_{\rm c}(^{16}{\rm O})$ are determined primarily by the uncertainties in these two reaction rates.

5.2.3. Triple-α and $^{12}C(\alpha, \gamma)^{16}O$

Figure 12 shows $X_{\rm c}(^{12}{\rm C})$ at He-depletion for the solar models as a function of the rate multiplier at maximum $f.u.$ (over core He-burning temperatures) applied to the ^{12}C(α, γ)^{16}O and triple-α rates (see Figure 2). A ^{12}C(α, γ)^{16}O rate that is small relative to its median value and a triple-α rate that is large relative to its median value produce a large $X_{\rm c}(^{12}{\rm C})$. Conversely, a high ^{12}C(α, γ)^{16}O rate and a small triple-α rate produce a small $X_{\rm c}(^{12}{\rm C})$. When both rates are at the median value of their respective PDFs, i.e., unity rate multipliers in Figure 12, $X_{\rm c}(^{12}{\rm C}) \simeq 0.26$ (see Figure 10). The trend is commensurate with West et al. (2013, their Figure 20).

5.2.4. Impact of the Measurement Point

Core He-burning is initiated by the triple-α reaction releasing $\approx$7.27 MeV of energy. At early times, nuclear energy generation in the core is governed by this reaction rate. The emergence of fresh ^{12}C as a product of the triple-α reaction allows ^{12}C(α, γ)^{16}O to convert the ^{12}C ashes into ^{16}O in a race between the two reactions to consume the He fuel (e.g., deBoer et al. 2017). The ^{12}C/^{16}O ratio is determined by these two reaction rates.

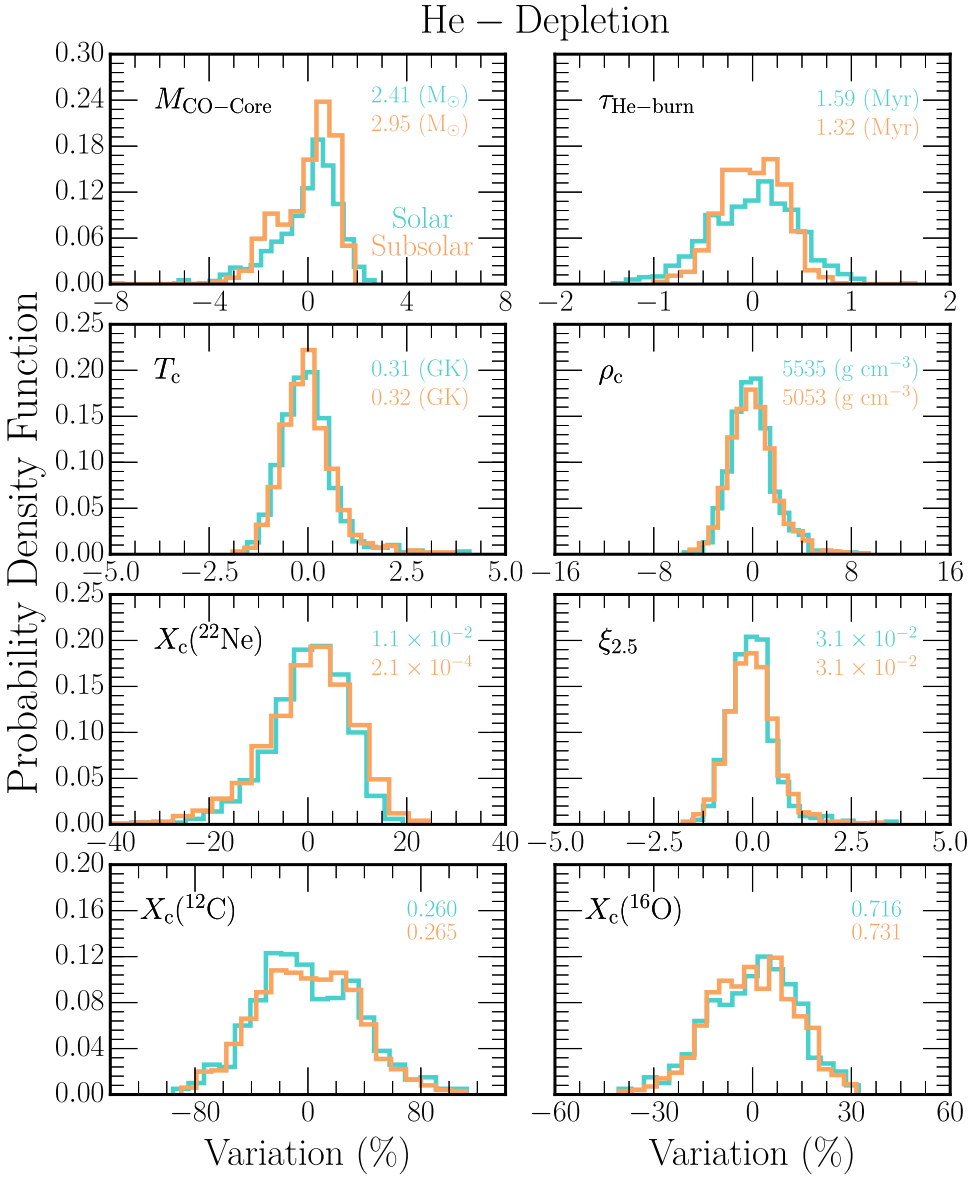

Figure 10. Same as in Figure 7 except we consider $M_{\rm CO\text{-}Core}$—the mass of the CO core, $\tau_{\rm He\text{-}burn}$—the elapsed time between H-depletion and He-depletion, $T_{\rm c}$—the central temperature, $\rho_{\rm c}$—the central density, $X_{\rm c}(^{22}{\rm Ne})$—the central neon-22 mass fraction, $\xi_{2.5}$—the compactness parameter, $X_{\rm c}(^{12}{\rm C})$—the central carbon-12 mass fraction, and $X_{\rm c}(^{16}{\rm O})$—the central oxygen-16 mass fraction, all measured at He-depletion.

Due to this evolution, we re-evaluate our SROC coefficients midway through the core He-burning process, when $X_{\rm c}(^4{\rm He}) \simeq 0.5$. The structural properties—$T_{\rm c}$, $\rho_{\rm c}$, and $\xi_{2.5}$—agree qualitatively when comparing the midway and depletion points of the solar models. A midway measurement point yields $\simeq$15% stronger correlations. The triple-α rate still drives the variations with a negative SROC. For $X_{\rm c}(^{12}{\rm C})$ and $X_{\rm c}(^{16}{\rm O})$ the midway and He-depletion measurement points for the solar models differ by $\Delta|r_{\rm s}| \lesssim 2\%$ in the SROC values.

When measuring midway through the core He-burning process, variations in $\tau_{\rm He\text{-}burn}$ for the solar models become mainly driven by the $^{14}{\rm N(p,}\,\gamma)^{15}{\rm O}$ rate with a positive SROC coefficient. An increase in this rate causes the stellar core to proceed through core H-burning at lower $T_{\rm c}$. When measuring $\tau_{\rm He\text{-}burn}$ midway through He-burning, we find that the $^{14}{\rm N(p,}\,\gamma)^{15}{\rm O}$ rate also yields a negative SROC coefficient for $T_{\rm c}$. Models with lower $T_{\rm c}$ proceed through He-burning at a slower rate, hence increasing the helium-burning lifetime $\tau_{\rm He\text{-}burn}$.

5.3. Carbon Depletion

Next, we measure the integrated impact of the reaction rate uncertainties at the point when the central carbon mass fraction $X_{\rm c}(^{12}{\rm C}) \lesssim 1 \times 10^{-6}$.

5.3.1. Probability Distribution Functions

Figure 13 shows the PDFs of eight properties of the 15 $M_\odot$ models at C-depletion: mass of the ONe core $M_{\rm ONe\text{-}Core}$, the elapsed time between He-depletion and C-depletion $\tau_{\rm C\text{-}burn}$, central temperature $T_{\rm c}$, central density $\rho_{\rm c}$, central electron fraction $Y_{\rm e,c}$, compactness parameter $\xi_{2.5}$, central $^{16}{\rm O}$ mass fraction $X_{\rm c}(^{16}{\rm O})$, and central $^{20}{\rm Ne}$ mass fraction $X_{\rm c}(^{20}{\rm Ne})$.

The $M_{\rm ONe\text{-}Core}$ distribution has 95% CI variation limits of $\simeq +23\%$ and $\simeq -50\%$ for the solar and subsolar models. This is wider than the spread in the He core mass at H-depletion ($\simeq \pm 0.1\%$) or the CO core mass at He-depletion ($\simeq \pm 3\%$). We

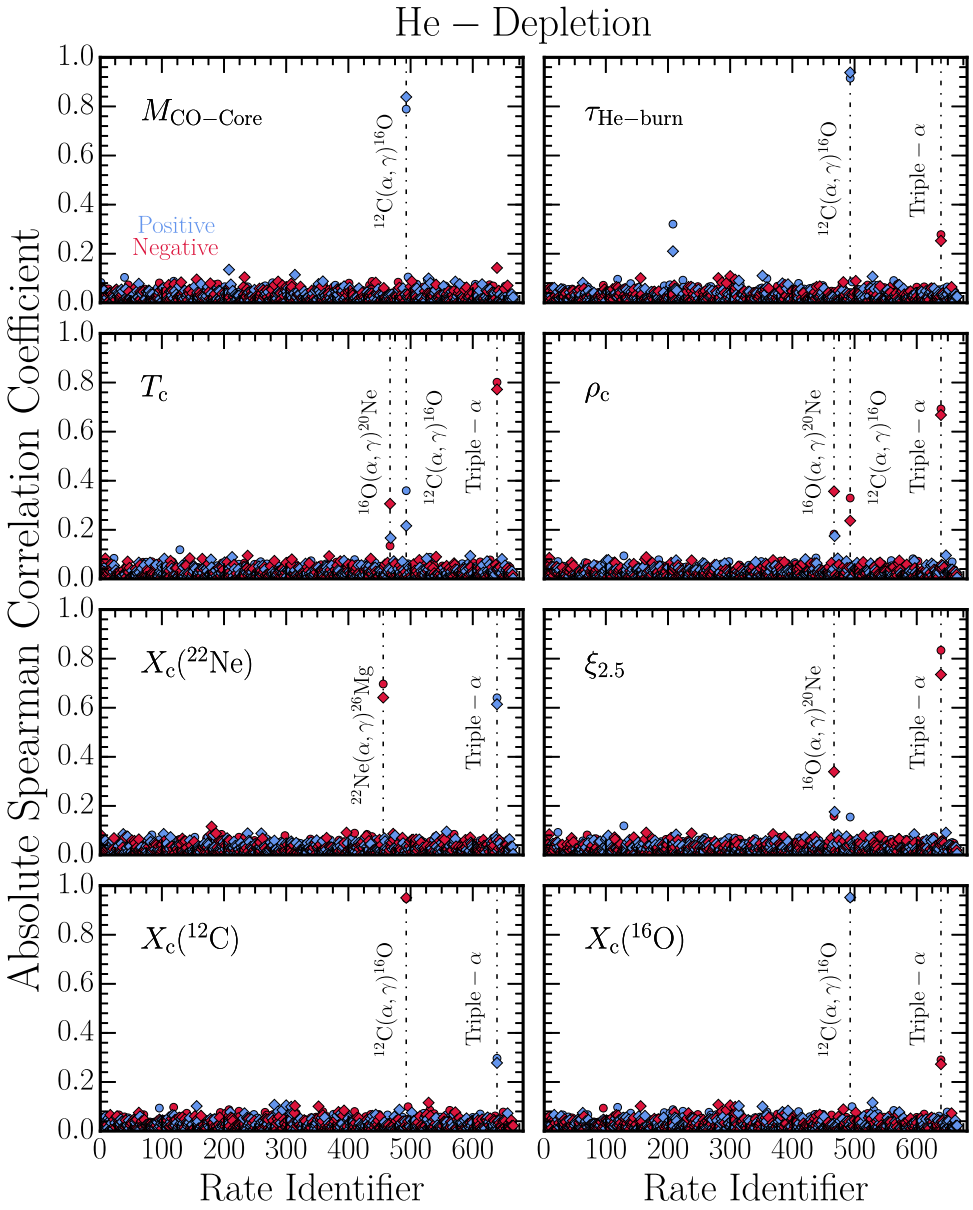

Figure 11. Same as in Figure 8. The quantities considered are $M_{\rm CO\text{-}Core}$—the mass of the CO core, $\tau_{\rm He\text{-}burn}$—the elapsed time between H-depletion and He-depletion, $T_{\rm c}$—the central temperature, $\rho_{\rm c}$—the central density, $X_{\rm c}(^{22}{\rm Ne})$—the central neon-22 mass fraction, $\xi_{2.5}$—the compactness parameter, $X_{\rm c}(^{12}{\rm C})$—the central carbon-12 mass fraction, and $X_{\rm c}(^{16}{\rm O})$—the central oxygen-16 mass fraction. All quantities used here were measured at He-depletion.

defer explanation to Section 5.3.3. In addition, the solar model PDF has a larger peak amplitude than the subsolar model PDF.

In contrast, the 95% CI spread of the $\tau_{\rm C\text{-}burn}$ distribution shows about the same narrow width of $\simeq \pm 1\%$ as $\tau_{\rm TAMS}$ and $\tau_{\rm He\text{-}burn}$. This is chiefly due to the CO core mass to be burned lying within a relatively narrow range ($\simeq \pm 3\%$, see Figure 10). The solar model PDF has a zero variance of $\tau_{\rm C\text{-}burn} \simeq 30.7$ kyr, while the subsolar model PDF has a zero variance of $\tau_{\rm C\text{-}burn} \simeq 23.8$ kyr. This reflects the subsolar model's undergoing hotter, less dense core C-burning (see Figure 4).

Carbon burning and the later stages of evolution in massive stars have large core luminosities whose energy is carried away predominantly by free-streaming neutrinos. These burning stages are thus characterized by short evolutionary timescales. When thermal neutrinos instead of photons dominate the energy loss budget, carbon and heavier fuels burn at a temperature chiefly set by the balanced power condition $\langle \epsilon_{\rm nuc} \rangle \simeq \langle \epsilon_{\nu} \rangle$. For core C-burning this gives $T_{\rm c} \simeq 0.9$ GK and, assuming a T^3/ρ scaling, $\rho_{\rm c} \simeq 6 \times 10^6$ g cm^{-3}. This is commensurate with the zero-variation values annotated in Figure 13. The $T_{\rm c}$ and $\rho_{\rm c}$ distributions show 95% CI widths of $\simeq \pm 15\%$ and $\simeq \pm 60\%$ for the solar and subsolar models, respectively. This is wider than the 95% CI spreads of the $T_{\rm c}$ and $\rho_{\rm c}$ distributions at H-depletion and He-depletion.

The $Y_{\rm e,c}$ distributions show strong peaks at $Y_{\rm e,c} \simeq 0.499$ and 95% CI spreads of $\lesssim 1\%$ for the solar and subsolar models. This is commensurate with significant neutronization not occurring during quiescent core C-burning, and shows that $Y_{\rm e,c}$ is not strongly affected by the uncertainties in the reaction rates.

C-depletion marks the first occurrence of significant variation in $\xi_{2.5}$. The solar and subsolar distributions show 95% CI widths of $\simeq \pm 16\%$. The mean value of $\xi_{2.5} \simeq 6.9 \times 10^{-2}$ for the solar models is smaller than the mean value of $\xi_{2.5} \simeq 8.6 \times 10^{-2}$ for the subsolar models. This

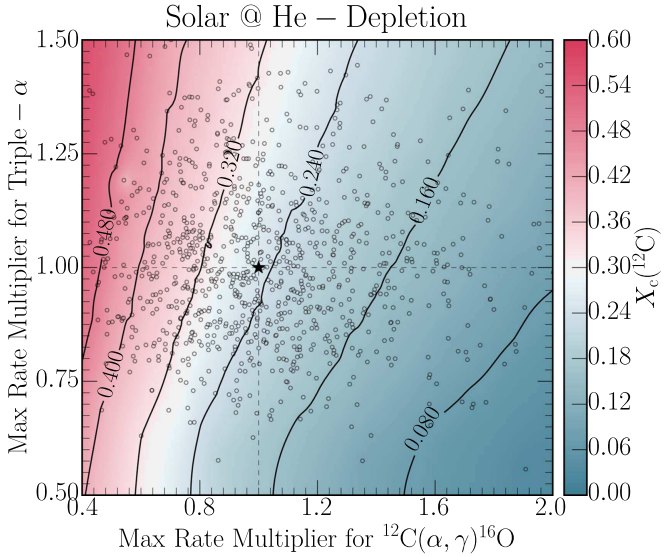

Figure 12. Central carbon mass fraction at helium depletion for solar models as a function of the rate multiplier at maximum *f.u.* applied to the $^{12}C(\alpha,\gamma)^{16}O$ and triple-α rates. The heat map uses bi-linear interpolation and extrapolation of the models, which are shown by gray circles. Contour lines of constant $X_c(^{12}C)$ are shown by solid black lines. Also shown, by a dashed line, is the value of a rate multiplier of unity for both reactions. Lastly, the black star denotes the value of $X_c(^{12}C)$ found for the *median* reaction rates. Compare with Figure 20 of West et al. (2013).

is due to the smaller ρ_c and shallower density gradient in the subsolar models than in the solar models.

The dominant isotopes at C-depletion are ^{16}O and ^{20}Ne. These two isotopes follow nearly Gaussian profiles with 95% CI spreads of $\simeq\pm40\%$ and $\simeq\pm70\%$ for $X_c(^{16}O)$ and $X_c(^{20}Ne)$, respectively. Despite this spread, the zero-variation values of ^{16}O and ^{20}Ne for the solar and subsolar models are within $\simeq1\%$.

5.3.2. Spearman Correlation Coefficients

Figure 14 shows the absolute SROCs for the 665 sampled reaction rates for the eight quantities considered in Figure 13 for the solar and subsolar grids of models.

Competition between the $^{12}C+^{12}C$ and $^{12}C+^{16}O$ reaction rates largely determines the mass of the ONe core at C-depletion. The $^{12}C(^{12}C,p)^{23}Na$ rate has significant positive SROC values of $r_s=(+0.58,+0.56)$ for the solar and subsolar models, respectively. Protons produced by $^{12}C(^{12}C,p)^{23}Na$ are usually captured by $^{23}Na(p,\alpha)^{20}Ne$, which increases $M_{\rm ONe\text{-}Core}$. Uncertainties in the $^{12}C(^{16}O,p)^{27}Al$ and $^{12}C(^{16}O,\alpha)^{24}Mg$ rates have significant negative SROC values, $r_s\simeq-0.40$, because the main products from these reactions ultimately produce ^{28}Si, which decreases $M_{\rm ONe\text{-}Core}$ by effectively transferring ^{16}O to ^{28}Si (Woosley et al. 1971; Fang et al. 2017; Martínez-Rodríguez et al. 2017).

The $^{12}C(\alpha,\gamma)^{16}O$ rate impacts the time between He-depletion and C-depletion $\tau_{\rm C\text{-}burn}$ with SROC values of $\simeq+0.91$ and $\simeq+0.94$ for the solar and subsolar models, respectively. This occurs because this rate sets the mass of the CO core, which has a relatively narrow 95% CI range of $\simeq\pm2\%$ (see Figure 10). Smaller uncertainties in the triple-α rate (negative correlation) and the $^{14}N(p,\gamma)^{15}O$ rate (positive correlation) occur because these two reactions play a diminished role in setting the mass of the CO core.

The SROC analysis for T_c and ρ_c shows dependences on the $^{12}C(\alpha,\gamma)^{16}O$, $^{12}C+^{12}C$, and $^{12}C+^{16}O$ rates for the solar and subsolar models. All these rates have negative SROCs of $r_s\simeq-0.4$. This magnitude and sign are partially due to thermal neutrino losses playing a key role in the evolution, and partially due to the thermostat mechanism, i.e., that reaction rates that produce greater energy yield cooler and less dense cores.

The quantities $Y_{e,c}$ and $\xi_{2.5}$ inherit a dependence on the $^{12}C(\alpha,\gamma)^{16}O$ rate from He-burning, with SROCs of $r_s\simeq(+0.7,+0.5)$, respectively. Uncertainties in the $^{12}C(^{12}C,p)^{23}Na$ and $^{12}C(^{16}O,p)^{27}Al$ rates also contribute with negative coefficients.

Likewise, $X_c(^{16}O)$ and $X_c(^{20}Ne)$ also inherit a strong dependence on the $^{12}C(\alpha,\gamma)^{16}O$ rate from He-burning, with SROCs of $r_s\simeq(+0.9,-0.8)$, respectively. $X_c(^{16}O)$ has a positive correlation coefficient because during He-burning a larger $^{12}C(\alpha,\gamma)^{16}O$ rate produces more ^{16}O. $X_c(^{20}Ne)$ has a negative SROC because a larger $^{12}C(\alpha,\gamma)^{16}O$ rate produces less ^{12}C, the principal fuel of C-burning, which produces less ^{20}Ne. Both isotopes also share a smaller dependence on the triple-α rate uncertainty, inherited from He-burning, and a small dependence on C-burning rates. These smaller dependences are also anticorrelated—increases in rates that increase $X_c(^{16}O)$ also decrease $X_c(^{20}Ne)$, and vice versa.

5.3.3. Impact of the Measurement Point

The 95% CI width of the $M_{\rm ONe\text{-}Core}$ PDF in Figure 13 is partly due to the measurement point. $M_{\rm ONe\text{-}Core}$ is still growing due to the episodes of off-center convective C-burning (see Figure 5). This contrasts with H and He, where convective core burning accounted for complete mixing of the ash of the nuclear burning.

In more detail, carbon ignites centrally and convectively in these $15M_\odot$ models. The extent of the convective core burning reaches $\simeq0.6\,M_\odot$. Convection retreats as carbon is depleted, and by $X_c(^{12}C)\simeq10^{-2}$ the entire core is radiative. Subsequently, the first off-center convective C-burning episode occurs when $X_c(^{12}C)\simeq10^{-4}$ and extends from $\simeq0.6\,M_\odot$ to $1.2-2.0\,M_\odot$ depending on the amount of C fuel available from core He-burning. It is the variability of the location and extent of the off-center convective C-burning episodes, which occur *before* the measurement point of $X_c(^{12}C)\lesssim1\times10^{-6}$, that drives the 95% CI spread in the $M_{\rm ONe\text{-}Core}$ PDF.

Figure 15 shows the impact of the measurement point on $M_{\rm ONe\text{-}Core}$ as a function of $X_c(^{12}C)$ for six solar grid models. The dashed vertical line shows our measurement point for C-depletion, $X_c(^{12}C)\lesssim1\times10^{-6}$. Given different compositions and thermodynamic trajectories inherited from core He-burning, some models are further along in transforming the CO core to an ONe core. Despite the 95% CI range in the $M_{\rm ONe\text{-}Core}$ PDF, our SROC analysis yields qualitatively similar results. Moreover, two models—the green and gold lines—grow larger ONe cores due to the extent of the convective zone of the final off-center C-burning episode mixing the fuel and ash of C-burning outward to a larger mass coordinate than the remaining three models.

5.4. Neon Depletion

Core Ne-depletion is the next evolutionary stage considered. We measure the integrated impact of the rate uncertainties at the point when the central neon mass fraction $X_c(^{20}Ne)\lesssim1\times10^{-3}$. This is a larger mass fraction than the 1×10^{-6} used for H-, He- and C-depletion. We use a larger depletion value

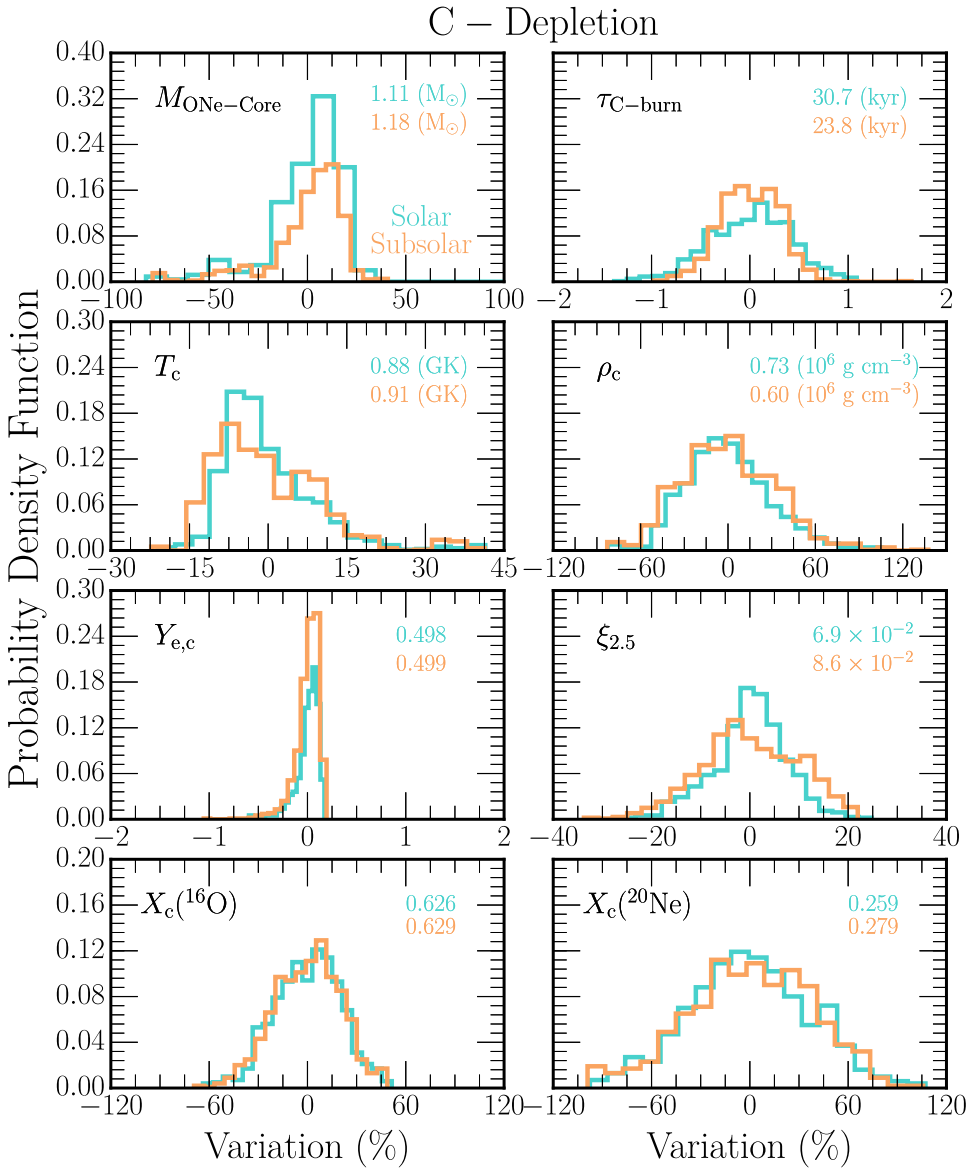

Figure 13. Same as in Figure 10 except we consider $M_{\rm ONe\text{-}Core}$—the mass of the ONe core, $\tau_{\rm C\text{-}burn}$—the elapsed time between He-depletion and C-depletion, $T_{\rm c}$—the central temperature, $\rho_{\rm c}$—the central density, $Y_{\rm e,c}$—the central electron fraction, $\xi_{2.5}$—the compactness parameter, $X_{\rm c}(^{16}{\rm O})$—the central oxygen-16 mass fraction, and $X_{\rm c}(^{20}{\rm Ne})$—the central neon-20 mass fraction. All quantities are measured at C-depletion.

because a growing convective core feeds unburned neon into the core. Ne does not deplete to 1×10^{-6} until well into core O-burning.

5.4.1. Probability Distribution Functions

Figure 16 shows the PDFs of eight properties of the stellar models at Ne-depletion. We consider the mass of the O core $M_{\rm ONe\text{-}Core}$, elapsed time between C-depletion and Ne-depletion $\tau_{\rm Ne\text{-}burn}$, central temperature $T_{\rm c}$, central density $\rho_{\rm c}$, central electron fraction $Y_{\rm e,c}$, compactness parameter $\xi_{2.5}$, central oxygen-16 mass fraction $X_{\rm c}(^{16}{\rm O})$, and central silicon-28 mass fraction and $X_{\rm c}(^{28}{\rm Si})$.

The $M_{\rm ONe\text{-}Core}$ PDF shows a strong peak for the solar and subsolar models, with zero-variation values of 1.44 $M_\odot$ and 1.49 $M_\odot$, respectively. The 95% CI spread is $\simeq\pm30\%$ for both sets of models. The peaks are offset from zero due to the long tail of positive variations. The $\tau_{\rm Ne\text{-}burn}$ PDFs show 95% CIs of $\simeq\pm1\%$, commensurate with $\tau_{\rm C\text{-}burn}$ in Figure 13. The 95% CI spread of the solar grid is slightly larger than the spread for the subsolar grid. Both PDFs are symmetric about zero variations of 10.1 yr and 8.10 yr, respectively.

The $T_{\rm c}$ distribution has zero-variation values of 1.60 GK and 1.63 GK for the solar and subsolar grids, respectively. Both PDFs are symmetric about their zero-variation values and have 95% CI widths of $\simeq\pm6\%$. The $\rho_{\rm c}$ PDF has zero-variation values of $5.12 \times 10^6\,{\rm g\,cm^{-3}}$ and $4.42 \times 10^6\,{\rm g\,cm^{-3}}$ for the solar and subsolar grids, respectively. Both PDFs have 95% CI widths of $\simeq \pm$ 50%. The subsolar model PDF has a slight bimodality with equal peaks of $\simeq$18%. The $T_{\rm c}$ and $\rho_{\rm c}$ PDFs have 95% spreads that are smaller than the corresponding 95% CI widths for C-depletion.

The $Y_{\rm e,c}$ PDFs for both metallicity grids peak strongly about their means, 0.498 and 0.499 respectively, with a 95% spread of $\lesssim$0.25%. This is about the same 95% CI spread as at C-depletion, reflecting that significant neutronization does not occur during Ne-burning. The $\xi_{2.5}$ PDF shows a 95% CI spread

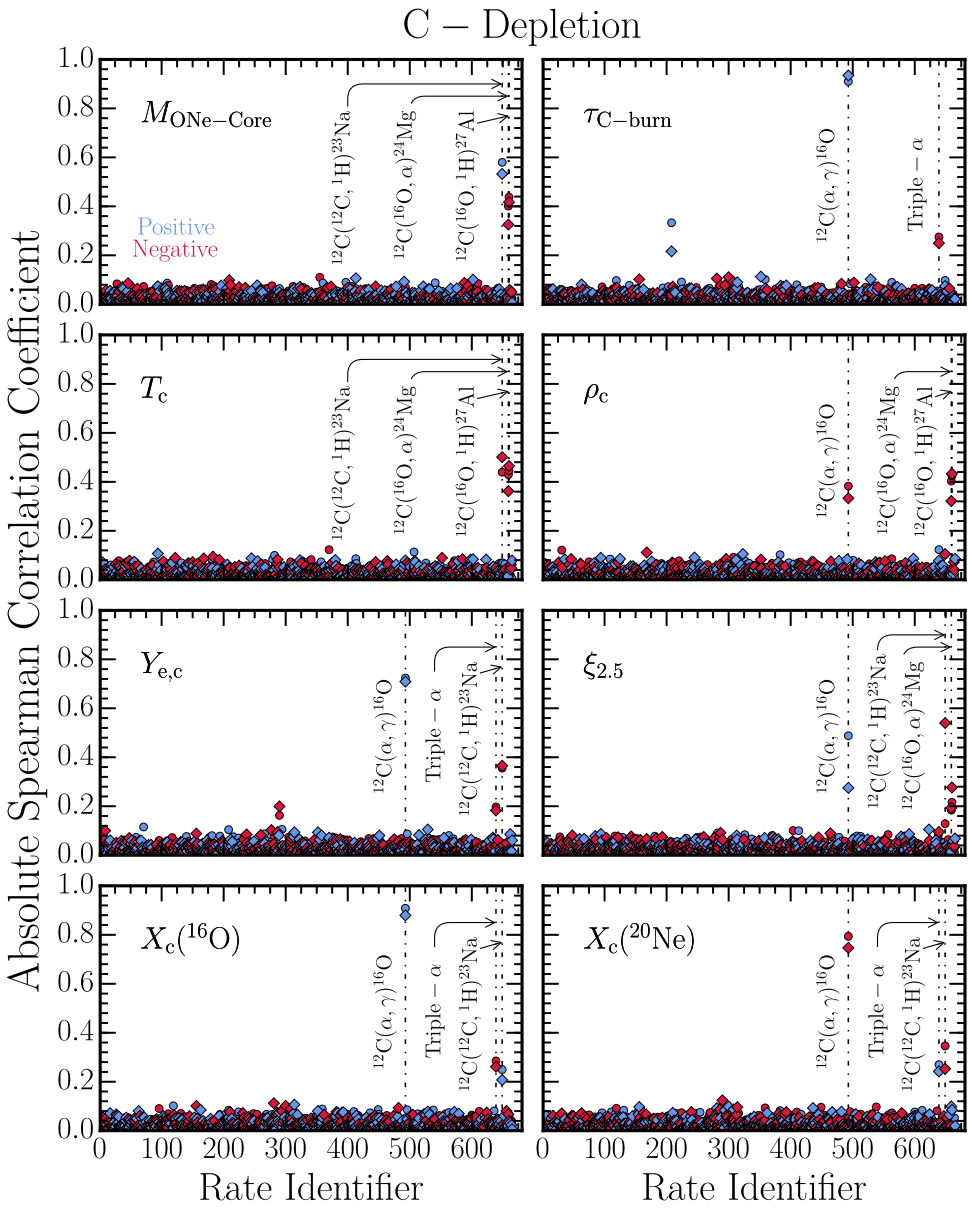

Figure 14. Same as in Figure 10 except we consider $M_{\rm ONe\text{-}Core}$—the mass of the ONe core, $\tau_{\rm C\text{-}burn}$—the elapsed time between He-depletion and C-depletion, $T_{\rm c}$—the central temperature, $\rho_{\rm c}$—the central density, $Y_{\rm e,c}$—the central electron fraction, $\xi_{2.5}$—the compactness parameter, $X_{\rm c}(^{16}{\rm O})$—the central oxygen-16 mass fraction, and $X_{\rm c}(^{20}{\rm Ne})$—the central neon-20 mass fraction. All quantities are measured at C-depletion.

of $\simeq \pm 20\%$ without a strong central peak for both metallicity grids.

$X_{\rm c}(^{16}{\rm O})$ follows a broad distribution about the mean with variations of $\simeq(+20\%, -30\%)$. In contrast, $X_{\rm c}(^{28}{\rm Si})$, the other dominant isotope at Ne-depletion, follows a more centrally peaked distribution but with a larger width of $\simeq -120\%$ and a slight, long tail showing variations out to $\simeq +200\%$ of the mean.

5.4.2. Spearman Correlation Coefficients

Figure 17 shows the SROC correlations for the eight quantities considered in Figure 16. Markers and colors are the same as in Figure 14.

Ne-depletion inherits most of the reaction rate dependences from He-depletion and C-depletion. This is consistent with Ne-burning being a photodisintegration rearrangement, whose net reaction is $2(^{20}{\rm Ne}) \rightarrow {}^{16}{\rm O} + {}^{24}{\rm Mg} + 4.6$ MeV. The nucleosynthesis products also resemble those at C-depletion but lack ^{23}Na and have more of the heavier nuclei ^{26,27}Al, ^{29,30}Si, and ^{31}P.

The 95% CI spread of $M_{\rm ONe\text{-}Core}$ is mainly driven by rate uncertainties in $^{12}{\rm C}(^{12}{\rm C},\,{\rm p})^{23}{\rm Na}$, with $r_{\rm s} \simeq +0.8$ for both metallicity grids. The $^{12}{\rm C}(\alpha,\,\gamma)^{16}{\rm O}$ rate also affects the O core mass but to a lesser extent, with $r_{\rm s} \simeq +0.4$. The 95% CI variation of $\tau_{\rm Ne\text{-}burn}$ follows that of the spread of $\tau_{\rm C\text{-}burn}$. It is affected primarily by uncertainties in the $^{12}{\rm C}(\alpha,\,\gamma)^{16}{\rm O}$ rate with smaller dependences on rate uncertainties in $^{14}{\rm N}({\rm p},\,\gamma)^{15}{\rm O}$ (positive SROC) and triple-α (negative SROC). In general, the SROC values are larger for the solar grid.

The $T_{\rm c}$ PDF depends mostly on the uncertainties in the $^{12}{\rm C}(\alpha,\,\gamma)^{16}{\rm O}$ rate for both solar and subsolar grids. The positive SROC implies that a larger $^{12}{\rm C}(\alpha,\,\gamma)^{16}{\rm O}$ rate yields a hotter stellar core. This is the first occurrence of an inversion of

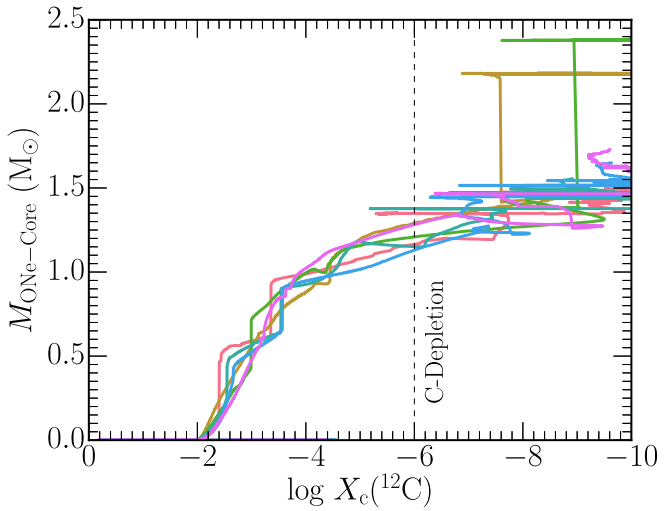

Figure 15. Mass of the ONe core as a function of the central ^{12}C mass fraction for six solar grid models. Our adopted measurement point for C-depletion, $X_c(^{12}C) \lesssim 1 \times 10^{-6}$, is shown by the dashed vertical line. Variation in the mass of the ONe core is driven by the size and extent of off-center convective C-buming episodes.

the thermostat mechanism. A small dependence is also found for the triple-α and the $^{12}C(^{12}C, p)^{23}Na$ rates.

The central density has an SROC value of $r_s \simeq +0.5$ for the $^{12}C(^{12}C, p)^{23}Na$ rate. However, ρ_c is also affected by uncertainties in the $^{16}O(^{16}O, p)^{31}P$ rate with $r_s \simeq -0.3$. This indicates that O-burning is beginning to take place at Ne-depletion. There is also a weaker dependence on the $^{16}O(^{16}O,^4He)^{28}Si$ rate with a negative SROC.

Uncertainties in the $^{12}C(\alpha, \gamma)^{16}O$ rate drive the variations in $Y_{e,c}$ and $\xi_{2.5}$ with SROC values of $r_s \simeq +0.6$. Smaller SROCs are also found for $Y_{e,c}$ and the 95% CI $^{27}Al(\alpha, p)^{30}Si$, triple-$\alpha$, $^{16}O(^{16}O, p)^{31}P$, $^{16}O(^{16}O, n)^{31}S$, and $^{12}C(^{12}C, p)^{23}Na$ rates. Similar to ρ_c, the compactness of the stellar core is weakly affected by the uncertainties inherited from the $^{12}C(^{12}C, p)^{23}Na$ rate.

$X_c(^{16}O)$ inherits a dependence on the $^{12}C(\alpha, \gamma)^{16}O$ rate with $r_s \simeq +0.7$ for both metallicity grids. The $^{12}C + ^{12}C$ and $^{16}O + ^{16}O$ rates have smaller, competing effects on $X_c(^{16}O)$ with $|r_s| \simeq 0.25$. $X_c(^{28}Si)$ is slightly anticorrelated with $X_c(^{16}O)$, with the $^{12}C(\alpha, \gamma)^{16}O$ rate having the largest (negative) SROC. Smaller effects from the uncertainties in the heavy-ion, carbon, and oxygen channels also play a role in its variation.

5.4.3. Impact of the Measurement Point

Some of the quantities measured at Ne-depletion partly inherit their 95% CI spread from the spread at C-depletion. However, the spread of most quantities at Ne-depletion is larger than the 95% CI spreads at C-depletion because of the thermodynamic conditions imposed by the depletion of carbon.

Figure 15 shows that the extent of the ONe core measured at C-depletion is sensitive to the extent of the final off-center convective carbon episode. Figure 18 shows $M_{\rm ONe-Core}$ as a function of the central ^{20}Ne mass fraction for the same six solar grid models as in Figure 15. The same two stellar models that yield larger ONe core masses in Figure 15 introduce larger 95% CI variations in the O core mass measured at Ne-depletion. The variation in the ONe core mass inherited from C-depletion can cause variations in the other measured quantities. We stress that our analysis measures the integrated impact of the reaction rate uncertainties on the evolution of the stellar model up to the measurement point.

5.5. Oxygen Depletion

The last evolutionary point we consider is core O-depletion, defined when $X_c(^{16}O) \lesssim 1 \times 10^{-3}$. We consider eight properties of the stellar model at this epoch: mass of the Si core $M_{\rm Ne\text{-}burn}$, time between Ne-depletion and O-depletion $\tau_{\rm O\text{-}burn}$, central temperature T_c, central density ρ_c, central electron fraction $Y_{e,c}$, compactness parameter $\xi_{2.5}$, central silicon-28 mass fraction $X_c(^{28}Si)$, and central sulfur-32 mass fraction $X_c(^{32}S)$.

5.5.1. Probability Distribution Functions

Figure 19 shows the variation of these quantities in the same format as for previous depletion epochs. The $M_{\rm Ne\text{-}burn}$ PDFs for the solar models span $\simeq -120$ to $+400$. Only the range ± 120 is shown in Figure 19. The full range, which is taken into account in the analysis, causes the peak to center at $\simeq -30\%$. Despite the wide range, the zero-variation values of $0.27\,M_\odot$ for the solar grid and $0.22\,M_\odot$ for the subsolar grid are similar. The 95% CI spreads are ≈ 4 times larger for O-depletion than for Ne-depletion for both the solar and subsolar grids.

The solar and subsolar $\tau_{\rm O\text{-}burn}$ PDFs have zero-variation values of 3.79 yr and 2.35 yr, respectively. The 95% CI spreads of $\simeq \pm 1\%$ are consistent with the 95% CI lifetimes of previous epochs. The subsolar model PDF has a slightly larger peak amplitude and smaller range.

The solar and subsolar T_c PDFs have a 95% CI width of $\simeq \pm 10\%$. The negative-variation tail causes a $\simeq -20\%$ shift away from the zero-variation values of 2.07 GK for the solar models and 2.14 GK for the subsolar models. The ρ_c PDFs have 95% CI spreads of $\simeq \pm 60\%$ with tails out to $\simeq +160\%$ for both metallicities. These tails cause the peak in the PDF to shift away from the arithmetic means of 23.3×10^6 g cm^{-3} for the solar models and 15.1×10^6 g cm^{-3} for the subsolar models. Commensurate with Figure 4, the solar models remain cooler and denser than the subsolar models at O-depletion.

At the elevated T_c and ρ_c that occur during O-depletion, the reactions $^{16}O(^{16}O, n)^{31}S$, $^{33}S(e^-,\nu)^{33}P$, $^{37}Ar(e^-,\nu)^{37}Cl$, and $^{35}Cl(e^-,\nu)^{35}S$ decrease $Y_{e,c}$. This is reflected in the $Y_{e,c}$ PDF having zero-variation values of 0.492 and 0.493 for the solar and subsolar grids, respectively. Peaks in the $Y_{e,c}$ PDF are shifted from these zero-variation values because both the solar and subsolar grids have tails of negative variations extending to $\simeq -2\%$.

The $\xi_{2.5}$ PDFs show 95% CI spreads of $\simeq \pm 20\%$ for the solar and subsolar grids. The arithmetic means of $\xi_{2.5} \simeq 0.102$ for the solar grid and $\xi_{2.5} \simeq 0.139$ for the subsolar grid are larger than the arithmetic means at Ne-depletion, but the difference in $\xi_{2.5}$ between the two metallicities is similar. The $X_c(^{28}Si)$ PDF is log-normal with a peak at $\simeq -45\%$ and extrema extending to variations of $\simeq -120\%$ and $\simeq +180\%$. The $X_c(^{32}S)$ PDF is broad with tails extending to $\simeq \pm 80\%$.

The 95% CI widths of the PDFs for $M_{\rm Ne\text{-}burn}$ are driven by the fact that the Si core is still forming at the measurement point of $X_c(^{16}O) \lesssim 1 \times 10^{-3}$. Additional dynamic range is introduced by some models forming heavier isotopes of Si and S, and MESA considering only ^{28}Si in the definition of the Si-core mass boundary. For example, the central composition at

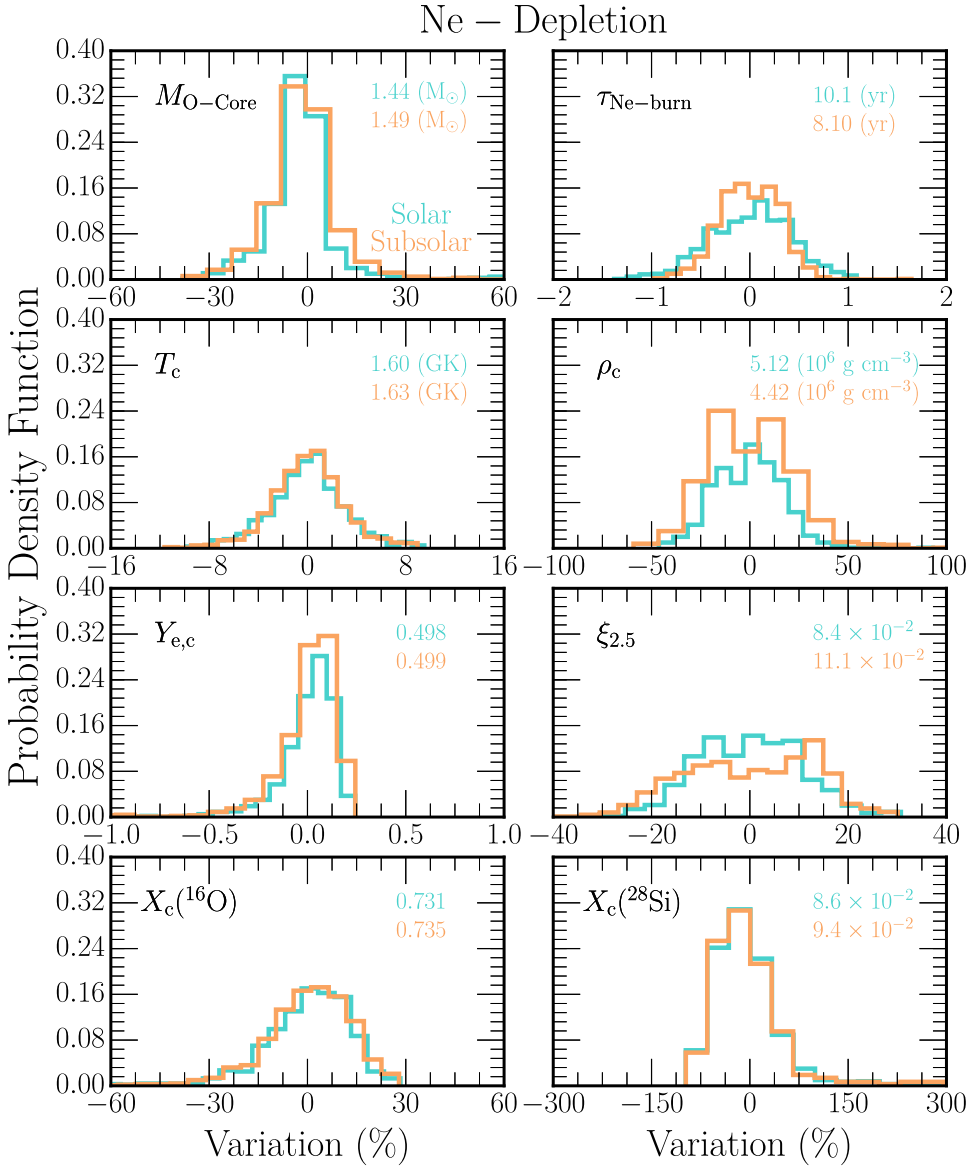

Figure 16. Same as in Figure 13 except we consider $M_{\rm ONe\text{-}Core}$—the mass of the O core, $\tau_{\rm Ne\text{-}burn}$—the elapsed time between C-depletion and Ne-depletion, $T_{\rm c}$—the central temperature, $\rho_{\rm c}$—the central density, $Y_{\rm e,c}$—the central electron fraction, $\xi_{2.5}$—the compactness parameter, $X_{\rm c}(^{16}{\rm O})$—the central oxygen-16 mass fraction, and $X_{\rm c}(^{28}{\rm Si})$—the central silicon-28 mass fraction. All quantities are measured at Ne-depletion.

O-depletion for one of the models in Figures 15 and 18 is $X_{\rm c}(^{28}{\rm Si}) \simeq 4.6 \times 10^{-2}$, $X_{\rm c}(^{30}{\rm Si}) \simeq 3.5 \times 10^{-1}$, $X_{\rm c}(^{32}{\rm S}) \simeq 4.6 \times 10^{-2}$, and $X_{\rm c}(^{34}{\rm S}) \simeq 4.4 \times 10^{-1}$. This model reports a very small $M_{\rm Ne\text{-}burn}$ because Si is primarily in the form of neutron-rich ^{30}Si. This also accounts for the negative tail in the $Y_{\rm e,c}$ PDF and the dynamic range in $\rho_{\rm c}$.

5.5.2. Spearman Correlation Coefficients

Figure 20 shows the SROC coefficients for the solar and subsolar grids against the eight quantities in Figure 19. The format is the same as in previous figures.

$M_{\rm Ne\text{-}burn}$ has a negative correlation of $r_{\rm s} \simeq -0.25$ with the $^{16}{\rm O}(^{16}{\rm O},\alpha)^{28}{\rm Si}$ rate and a smaller dependence on the $^{12}{\rm C}(\alpha,\gamma)^{16}{\rm O}$ rate. Reaction rates whose uncertainty most impacts $\tau_{\rm O\text{-}burn}$ are inherited from previous stages, namely $^{12}{\rm C}(\alpha,\gamma)^{16}{\rm O}$, $^{14}{\rm N}({\rm p},\gamma)^{15}{\rm O}$, and triple-$\alpha$.

$T_{\rm c}$ has a negative correlation with the $^{16}{\rm O}(^{16}{\rm O},{\rm n})^{31}{\rm S}$ rate for the solar and subsolar grids. $\rho_{\rm c}$ inherits its dependence on the $^{12}{\rm C}(\alpha,\gamma)^{16}{\rm O}$ rate with $r_{\rm s} \simeq -0.45$. The other $^{16}{\rm O}+^{16}{\rm O}$ exit channels have smaller effects on $T_{\rm c}$ and $\rho_{\rm c}$. The $^{16}{\rm O}(^{16}{\rm O},{\rm n})^{31}{\rm S}$ rate dominates the SROCs for $Y_{\rm e,c}$ with $r_{\rm s} \simeq -0.6$ for both grids. $\xi_{2.5}$ inherits dependences on the $^{12}{\rm C}(\alpha,\gamma)^{16}{\rm O}$ and $^{12}{\rm C}(^{12}{\rm C},{\rm p})^{23}{\rm Na}$ rates. The mass fractions $X_{\rm c}(^{28}{\rm Si})$ and $X_{\rm c}(^{32}{\rm S})$ are chiefly the result of the competition between the $^{16}{\rm O}(^{16}{\rm O},\alpha)^{28}{\rm Si}$ and $^{28}{\rm Si}(\alpha,\gamma)^{32}{\rm S}$ rates.

Table 1 summarizes the properties of the PDFs and the SROC analysis at O-depletion, along with the results for previous depletion points of the major fuels.

6. Discussion

Figure 21 shows the 95% CI variations listed in Table 1 for seven properties across five evolutionary epochs for the solar and subsolar grids. Across these properties, the magnitude of the 95% CI spreads generally grows with each successive stage of evolution. The variations grow for two reasons: (i) each evolutionary stage inherits variations from the previous

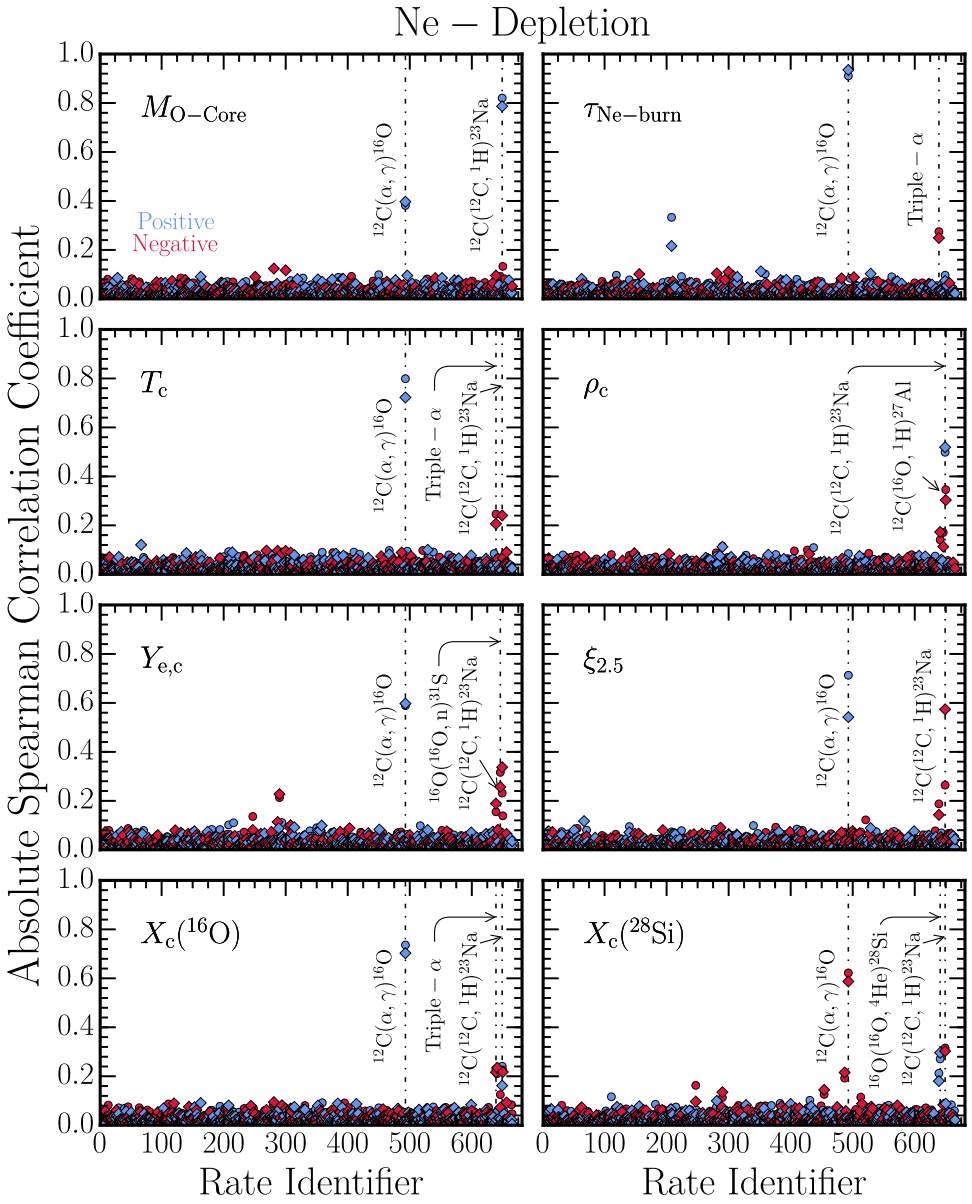

Figure 17. Same as in Figure 14. The quantities considered are $M_{\rm ONe\text{-}Core}$—the mass of the O core, $\tau_{\rm Ne\text{-}burn}$—the elapsed time between C-depletion and Ne-depletion, $T_{\rm c}$—the central temperature, $\rho_{\rm c}$—the central density, $Y_{\rm e,c}$—the central electron fraction, $\xi_{2.5}$—the compactness parameter, $X_{\rm c}(^{16}{\rm O})$—the central oxygen-16 mass fraction, and $X_{\rm c}(^{28}{\rm Si})$—the central silicon-28 mass fraction. All quantities are measured at Ne-depletion.

evolutionary stage because we measure the integrated impact of the uncertainties in the reaction rates; (ii) each stage imprints its own contributions to the variations due to the uncertainties in the specific reaction rates that impact that stage. Finally, there is a trend for the 95% CI variations of the subsolar models to be smaller than the variations of the solar models, particularly for measurements at H-, He- and C-depletion.

We next discuss the reaction rates identified in Table 1 that have the largest impact on the variations of the core mass, burning lifetime, composition, and structural properties.

6.1. Key Reaction Rates

At H-depletion, Table 1 shows that the uncertainties from the $^{14}{\rm N(p,\gamma)^{15}O}$ reaction rate cause 95% CI variations of $\approx\pm0.1\%$ in $M_{\rm He\text{-}Core}$, $\approx\pm0.2\%$ in $\tau_{\rm TAMS}$, $\approx\pm1\%$ in $T_{\rm c}$, $\approx\pm3\%$ in $\rho_{\rm c}$, $\approx\pm1\%$ in $\xi_{2.5}$, and $\approx\pm1\%$ in $X_{\rm c}(^{14}{\rm N})$ for both solar and subsolar models. The $^{14}{\rm N(p,\gamma)^{15}O}$ reaction rate is the slowest step in the CNO cycle and thus determines the rate at which H is depleted in the core (e.g., Iliadis 2007). STARLIB currently adopts the reaction rate of Imbriani et al. (2005).

The lowest positive-energy resonance of $^{14}{\rm N(p,\gamma)^{15}O}$ is located at a center-of-mass energy of 259 keV, too high in energy to strongly influence quiescent stellar burning (e.g., LUNA Collaboration et al. 2006). However, the strength of this resonance is often used as a cross-section normalization for lower-energy measurements. Daigle et al. (2016) report measurements of the energy, strength, and γ-ray branching ratios for the 259 keV resonance. Their recommended strength of $\omega\gamma = 12.6$ MeV is in agreement with the previous value but more precise, and offers a more reliable normalization. Using this result, they suggest that the S-factor data of Imbriani et al. (2005) should be reduced by 2.3%. For this reduction of the S-factor, the largest variation in our stellar models at

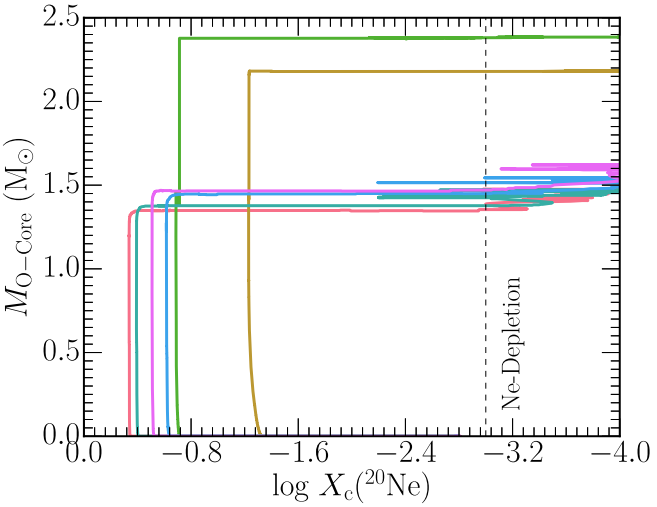

Figure 18. Mass of the O core as a function of the central ^{20}Ne mass fraction for the same six solar grid models as in Figure 15. Our adopted measurement point for Ne-depletion, $X_{\rm c}(^{20}{\rm Ne}) \lesssim 1 \times 10^{-3}$, is shown by the dashed vertical line. Variation in the mass of the O core is driven by the extent of the final off-center C flash prior to Ne-depletion.

H-depletion is ≈+0.2% with respect to the mean for $\rho_{\rm c}$. Other properties have variations ≲0.1%.

STARLIB currently adopts the triple-α reaction rate of Angulo et al. (1999). Uncertainties in this reaction rate dominate the 95% CI variations of ≈±1.5% in $T_{\rm c}$, ≈±3.5% in $\rho_{\rm c}$, and ≈ ±3.5% in $\xi_{2.5}$ during core He-burning. Nguyen et al. (2012) combine Faddeev hyperspherical harmonics and the *R*-matrix method to suggest that the triple-α reaction rate is significantly enhanced at temperatures below 0.06 GK. For an increased reaction rate in this temperature range, our analysis suggests that $T_{\rm c}$ and $\rho_{\rm c}$ will decrease by ≈2% in our MESA models.

STARLIB currently adopts the reaction rate of Kunz et al. (2002) for $^{12}{\rm C}(\alpha,\gamma)^{16}{\rm O}$. Experimental uncertainties in this reaction rate dominate the 95% CI variations of ≈2.5% in $M_{\rm CO\text{-}Core}$, ≈±1% in $\tau_{\rm He\text{-}burn}$, ≈+80%/−70% in $X_{\rm c}(^{12}{\rm C})$, and ≈+25%/−27% in $X_{\rm c}(^{16}{\rm O})$ during core He-burning. Core C-, Ne-, and even O-burning inherit some of these dependences. deBoer et al. (2017) use the *R*-matrix method to derive a new $^{12}{\rm C}(\alpha,\gamma)^{16}{\rm O}$ rate. The uncertainties in their new rate are smaller than the uncertainties in that of Kunz et al. (2002) near temperatures of $0.05 \lesssim T \lesssim 1$ GK and slightly larger near $T \simeq$ 1–3 GK. deBoer et al. (2017) show that their rate can lead to changes of $\simeq \pm 1.5\%$ for $M_{\rm CO\text{-}Core}$ in their $15M_\odot$ solar metallicity MESA models. This is slightly smaller than our 95% CI spread.

STARLIB adopts the $^{12}{\rm C}+^{12}{\rm C}$, $^{12}{\rm C}+^{16}{\rm O}$, and $^{16}{\rm O}+^{16}{\rm O}$ rates and branching ratios of Caughlan & Fowler (1988). Uncertainties in these reaction rates and branching ratios dominate the 95% CI variations of ≈+23%/−50% in $M_{\rm ONe\text{-}Core}$ at C-depletion and ≈+40%/−35% in $\rho_{\rm c}$ at Ne-depletion.

$^{12}{\rm C}+^{12}{\rm C}$ is one of the most studied heavy-ion reactions. Despite several decades of dedicated experimental efforts, the low-energy reaction rate still carries considerable uncertainties due to pronounced resonance structures that are thought to be associated with molecular configurations of carbon in the ^{24}Mg excited state (e.g., Mişicu & Esbensen 2007) However, it has been argued that the low-energy cross section of fusion reactions declines faster with decreasing energy than projected by common potential models (Gasques et al. 2007; Jiang et al. 2007a; Carnelli et al. 2014).

The impact of changes in the $^{12}{\rm C}+^{12}{\rm C}$ rate in 1D Geneva stellar evolution (GENEC) models is investigated in Bennett et al. (2012) and Pignatari et al. (2013). They find that an increase in the $^{12}{\rm C}+^{12}{\rm C}$ reaction rate causes core C-burning ignition at a lower temperature. This reduces the thermal neutrino losses, which in turn increases the core C-burning lifetime. They also find that an increased $^{12}{\rm C}+^{12}{\rm C}$ rate increases the upper initial mass limit for when a star undergoes convective C-burning rather than radiative C-burning (Lamb et al. 1976; Woosley & Weaver 1986; I. Petermann et al. 2017, in preparation). The subsequent evolution of these more massive stars may yield a bimodal distribution of compact objects (Timmes et al. 1996; Zhang et al. 2008; I. Petermann et al. 2017, in preparation).

Fang et al. (2017) use a high-intensity oxygen beam impinging upon an ultrapure graphite target to make new measurements of the total cross section and branching ratios for the $^{12}{\rm C}+^{16}{\rm O}$ reaction. They find a new broad resonance-like structure and a decreasing trend in the *S*-factor data toward lower energies, in contrast to previous measurements. For massive stars, they conclude that the impact of the new $^{12}{\rm C}+^{16}{\rm O}$ rate might be small for core and shell burning (also see Jiang et al. 2007b), although the impact might be enhanced by multidimensional turbulence (Cristini et al. 2017) or rotation (Chatzopoulos et al. 2016a) of the pre-supernova star during the last phases of its stellar life.

Of the key nuclear reaction rates identified in this study, those with the largest uncertainty over the temperature ranges considered here are heavy-ion $^{12}{\rm C}+^{12}{\rm C}$, $^{12}{\rm C}+^{16}{\rm O}$, and $^{16}{\rm O}+^{16}{\rm O}$ reactions. Due to the larger Coulomb barrier for the $^{12}{\rm C}+^{16}{\rm O}$ reaction it is expected to be less efficient during carbon burning. Our results suggest that variation in this rate, especially the p exit channel, can lead to non-negligible variations in core temperature and density during carbon burning. Our results suggest that for a decrease in the uncertainty in these heavy-ion reactions rates over stellar temperatures, along with the $^{12}{\rm C}(\alpha,\gamma)^{16}{\rm O}$ reaction, we can expect a *decrease* in variation of stellar model properties of below the level of variations induced by uncertainties due to stellar winds, convective boundary mixing, and mass/network resolution.

6.2. Assessing the Overall Impact

Paper F16 applies the Monte Carlo framework to stellar models that form CO white dwarfs. They evolve $3M_\odot$ solar metallicity models from the pre-main sequence to the first thermal pulse. They sample 26 out of 405 nuclear reactions and consider one evolutionary epoch—the first thermal pulse, a time shortly after core He-depletion. Comparing our Figure 11 with their Figure 11, we find similar results despite the different masses. The $^{12}{\rm C}(\alpha,\gamma)^{16}{\rm O}$ reaction dominates the mass of the CO core. The ^{12}C and ^{16}O mass fractions at He-depletion (their first thermal pulse) have SROC coefficients of similar sign and magnitude. In agreement with their CO white dwarf models, variations in the central temperature are driven by uncertainties in the triple-α reaction rate. They report that the central density is primarily correlated with uncertainties in the $^{12}{\rm C}(\alpha,\gamma)^{16}{\rm O}$ rate, while we find that the variations in the central density are chiefly correlated with uncertainties in the triple-α rate. This

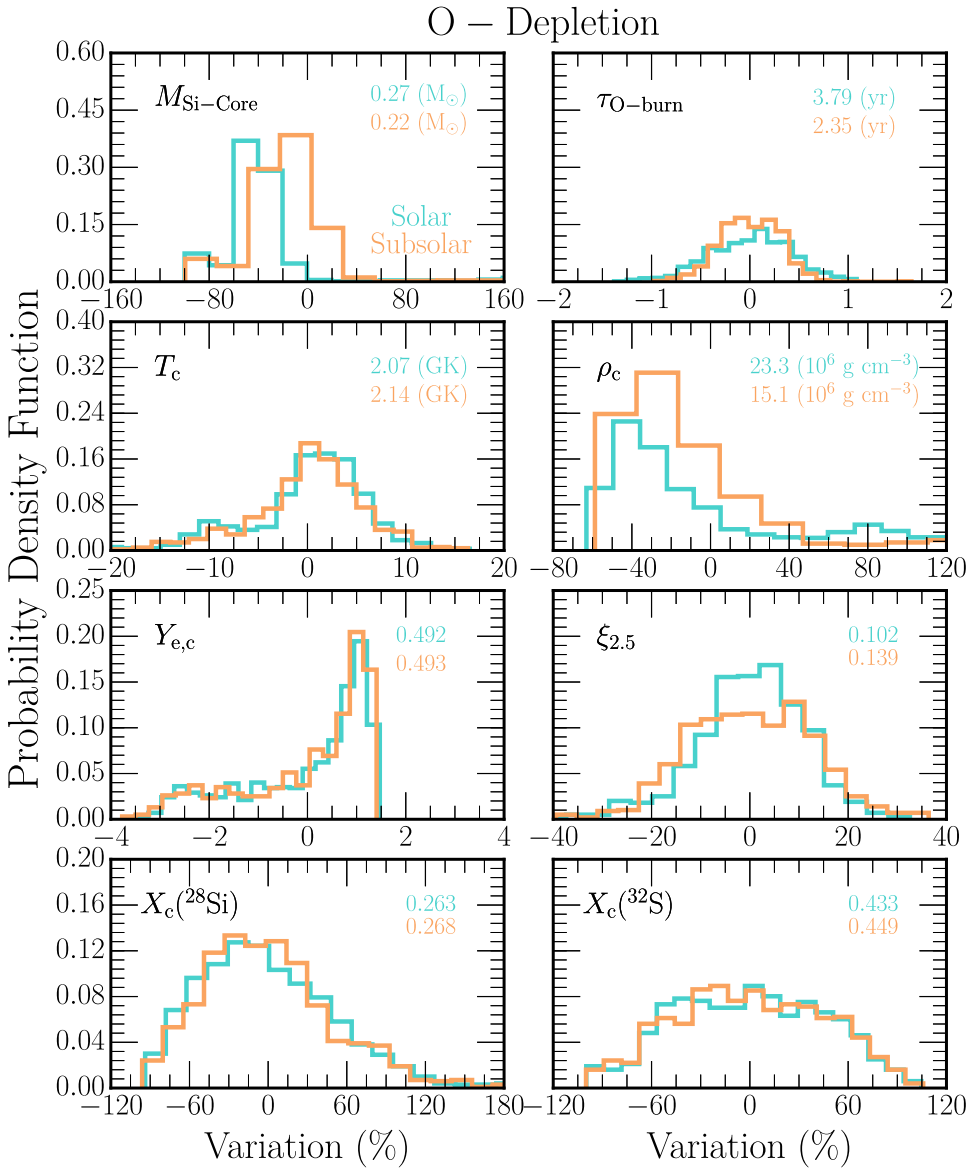

Figure 19. Same as in Figure 16 except we consider $M_{\rm Ne\text{-}burn}$—the mass of the Si core, $\tau_{\rm O\text{-}burn}$—the elapsed time between Ne-depletion and O-depletion, $T_{\rm c}$—the central temperature, $\rho_{\rm c}$—the central density, $Y_{\rm e,c}$—the central electron fraction, $\xi_{2.5}$—the compactness parameter, $X_{\rm c}(^{28}{\rm Si})$—the central silicon-28 mass fraction, and $X_{\rm c}(^{32}{\rm S})$—the central sulfur-32 mass fraction, all measured at O-depletion.

difference is due to the masses considered. The hotter, less dense, cores of our $15M_\odot$ models favor the triple-α rate as the primary source of the central density variations, whereas the cooler, denser $3M_\odot$ models favor $^{12}{\rm C}(\alpha,\gamma)^{16}{\rm O}$.

Farmer et al. (2016) explore uncertainties in the structure of models of massive stars with respect to mass resolution, mass loss, and the number of isotopes in the nuclear reaction network. Farmer et al. (2016) and this paper both report results for MESA r7624 models with $15M_\odot$, $\dot{M}\neq 0$, 127 isotopes, and solar metallicity. The primary difference between this paper and Farmer et al. (2016) is the use of STARLIB reaction rates.

Our results at H-depletion can be compared with their results at He-ignition. For example, Table 1 shows that our mean He core mass is $M_{\rm He\text{-}Core}=2.80\,M_\odot$ while their median He core mass is ${\rm He_{core}}=2.77\,M_\odot$, a difference of $\simeq$1%. Our 95% CI for $M_{\rm He-core}$ is within 1% of their upper and lower limits for ${\rm He_{core}}$. As another example, our mean H-burning lifetime is $\tau_{\rm TAMS}=11.27$ Myr and their median H-burning lifetime is $\tau_{\rm H}=10.99$ Myr, a difference of $\simeq$3%. In addition, our 95% CI for $\tau_{\rm TAMS}$ is $\simeq$2% larger than their upper and lower bounds for $\tau_{\rm H}$.

Our He-depletion results can also be compared to their results at C-ignition. We find a mean $M_{\rm C-Core}=2.41\,M_\odot$ while their median ${\rm C_{core}}=2.44\,M_\odot$, a difference of $\simeq$1%. Our 95% CI spread due to uncertainties in the nuclear reaction rates is $\simeq(+1.9\%,-3.1\%)$ while their upper and lower bounds suggest variations of $\simeq(+3.7\%,-0.4\%)$ due to changes in mass and network resolution. In addition, our mean $\tau_{\rm He\text{-}burn}=1.594$ Myr and their median $\tau_{\rm He}=1.74$ Myr, a difference of $\simeq$8%. Our 95% CI for $\tau_{\rm He\text{-}burn}$ is $\simeq(+1.9\%,-3.1\%)$ while their upper and lower bounds are $\simeq(+1.2\%,-12.1\%)$.

Comparing our Ne-depletion results with their O-ignition results, we find a mean $M_{\rm ONe\text{-}Core}=1.44\,M_\odot$ while their median ${\rm O_{core}}=1.40\,M_\odot$, a difference of $\lesssim$3%. Our 95% CI spread due to uncertainties in the nuclear reaction rates is $\simeq(+65\%,-23\%)$ while their upper and lower bounds suggest

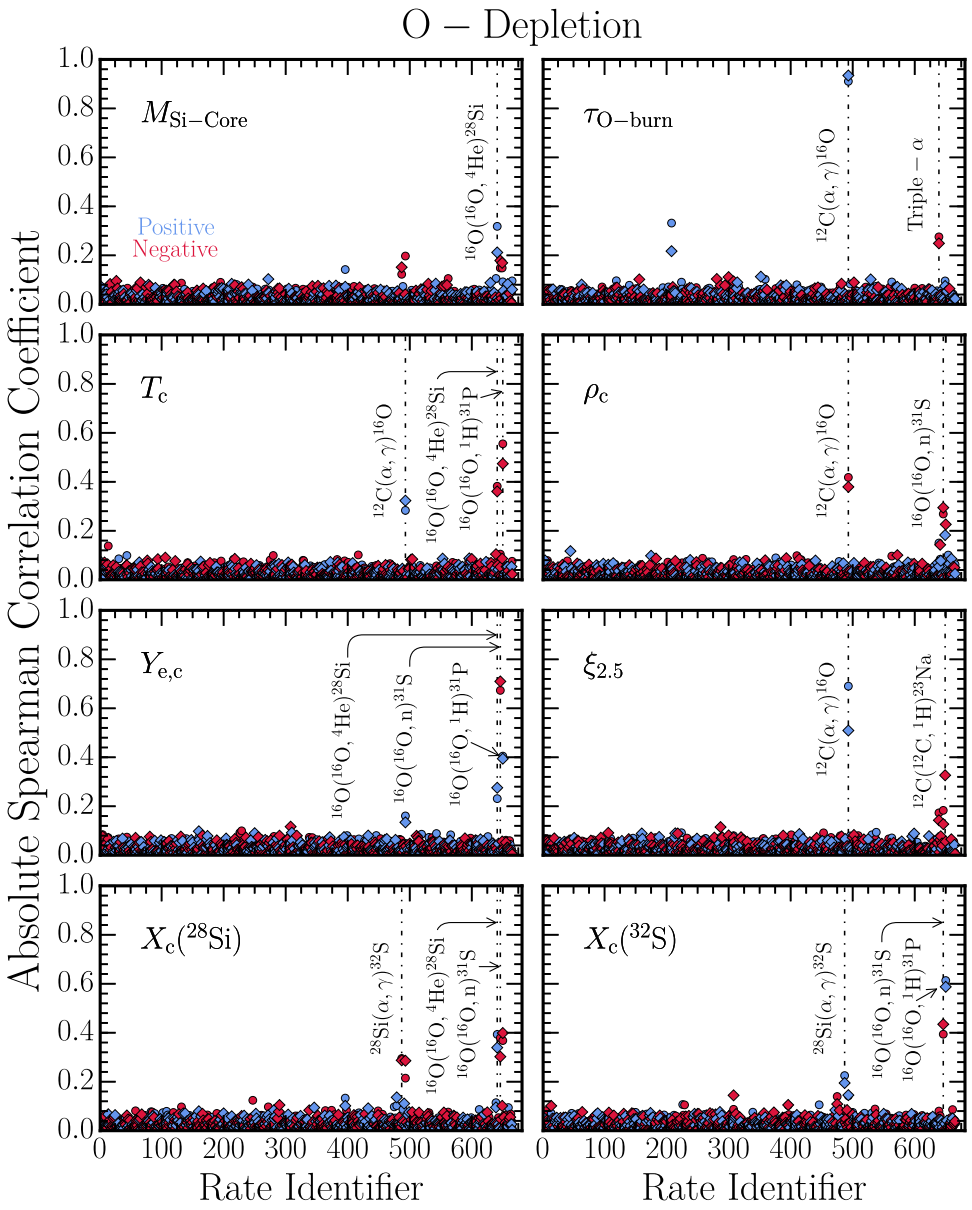

Figure 20. Same as in Figure 17. The quantities considered are $M_{\rm Ne\text{-}burn}$—the mass of the Si core, $\tau_{\rm O\text{-}burn}$—the elapsed time between Ne-depletion and O-depletion, $T_{\rm c}$—the central temperature, $\rho_{\rm c}$—the central density, $Y_{\rm e,c}$—the central electron fraction, $\xi_{2.5}$—the compactness parameter, $X_{\rm c}(^{28}{\rm Si})$—the central silicon-28 mass fraction, and $X_{\rm c}(^{32}{\rm S})$—the central sulfur-32 mass fraction. All quantities are measured at O-depletion.

variations of $\simeq(+0.1\%, -5.6\%)$ due to changes in mass and network resolution. In addition, our mean $\tau_{\rm C\text{-}burn} = 30.74$ kyr and their median $\tau_{\rm C} = 85.55$ yr differ by approximately three orders of magnitude. This large difference is due to the exact measurement points. In this work, we assumed the time to be the difference between the age of the star at C-depletion and its age at He-depletion. This does not necessarily correspond to the exact burning lifetime for C because the star undergoes reconfiguration after He-depletion for a few thousand years before conditions for C-burning are met. Farmer et al. (2016) measure the time to transition to the next major fuel source. Our 95% CI for $\tau_{\rm C\text{-}burn}$ is $\simeq(+1.9\%, -3.1\%)$, while their upper and lower bounds are $\simeq(+1.2\%, -12.1\%)$.

Variations in properties of stellar evolution models can be found to be caused by other sources of uncertainty beyond those discussed above. Renzo et al. (2017) considered uncertainties in the mass loss prescriptions and efficiencies used in non-rotating single stars of solar metallicity. They find that changes in these parameters can lead to a spread of $\Delta M_{\rm CO} \approx 0.28\,M_{\odot}$ in CO core masses measured at O-depletion, though this is defined differently in their work as the moment when $X_{\rm c}(^{16}{\rm O}) \lesssim 0.04$. This spread represents a variation of about $\pm 5\%$ about the arithmetic mean. The treatment of mixing at the convective boundaries can also have a significant effect on the evolution of massive stellar models. Davis et al. (2017) show that for their $25M_{\odot}$ model at Ne-ignition, they find a variation of $+5\%$ in the ONe core mass due to changes in the efficiency of convective boundary mixing at metal-burning interfaces.

Farmer et al. (2016) find that mass resolution has a larger impact on the variations than the number of isotopes up to and including C-burning, while the number of isotopes plays a more significant role in determining the span of the variations for Ne-, O-, and Si-burning. Comparisons of the core masses and burning lifetimes suggests that at H- and He-depletion, the

Table 1
Properties of 15 $M_\odot$ Solar and Subsolar Monte Carlo Stellar Models

Property	Solar			Subsolar			95% CI Limits of Variation (%)
	Values	Key Reaction	r_s	Values	Key Reaction	r_s	
H-Depletion							
$M_{\text{He-Core}}$ ($M_\odot$)	$2.802^{2.806}_{2.799}$	^{14}N(p, γ)^{15}O	+0.35	$2.86^{2.863}_{2.857}$	…	+0.33	(+0.13, −0.12) (+0.12,−0.12)
τ_{TAMS} (Myr)	$11.27^{11.29}_{11.249}$	^{14}N(p, γ)^{15}O	+1.0	$11.769^{11.78}_{11.759}$	…	+1.0	(+0.18,−0.19) (+0.09,−0.09)
T_c (10^8 K)	$0.628^{0.635}_{0.621}$	^{14}N(p, γ)^{15}O	−0.99	$0.807^{0.816}_{0.799}$	…	−0.99	(+1.19,−1.12) (+1.07,−1.11)
ρ_c (g cm^{-3})	$42.402^{43.917}_{40.978}$	^{14}N(p, γ)^{15}O	−0.97	$88.198^{91.241}_{85.122}$	…	−0.98	(+3.57,−3.36) (+3.45,−3.49)
$\xi_{2.5}$	$0.007^{0.007}_{0.007}$	^{14}N(p, γ)^{15}O	−0.99	$0.008^{0.009}_{0.008}$	…	−0.99	(+1.19,−1.14) (+1.09,−1.13)
$X_c(^{14}\text{N}) \times 10^3$	$9.234^{9.317}_{9.128}$	^{15}N(p, γ)^{16}O	−0.56	$0.194^{0.195}_{0.192}$	^{14}N(p, γ)^{15}O	−0.66	(+0.89,−1.15) (+0.83,−1.08)
He-Depletion							
$M_{\text{CO-Core}}$ ($M_\odot$)	$2.414^{2.522}_{2.347}$	^{12}C(α, γ)^{16}O	+0.79	$2.952^{3.062}_{2.909}$	…	+0.84	(+1.94,−3.10) (+1.53,−2.44)
$\tau_{\text{He-burn}}$ (Myr)	$1.594^{1.696}_{1.479}$	^{12}C(α, γ)^{16}O	+0.92	$1.315^{1.393}_{1.234}$	…	+0.94	(+0.81,−0.90) (+0.58,−0.63)
T_c (10^8 K)	$3.126^{3.185}_{3.092}$	Triple-α	−0.80	$3.207^{3.26}_{3.171}$	…	−0.77	(+1.89,−1.07) (+1.67,−1.11)
ρ_c (10^3 g cm^{-3})	$5.535^{5.756}_{5.364}$	Triple-α	−0.69	$5.053^{5.265}_{4.892}$	…	−0.67	(+3.99,−3.08) (+4.19,−3.20)
$X_c(^{22}\text{Ne}) \times 10^2$	$1.081^{1.217}_{0.887}$	^{22}Ne(α, γ)^{26}Mg	−0.70	$0.021^{0.024}_{0.017}$	…	−0.64	(+12.6,−17.9) (+15.5,−21.5)
$\xi_{2.5}$	$0.031^{0.031}_{0.03}$	Triple-α	−0.83	$0.031^{0.032}_{0.031}$	…	−0.74	(+1.56,−0.97) (+1.41,−1.06)
$X_c(^{12}\text{C})$	$0.260^{0.467}_{0.077}$	^{12}C(α, γ)^{16}O	−0.95	$0.265^{0.459}_{0.082}$	…	−0.95	(+79.9,−70.2) (+73.1,−69.1)
$X_c(^{16}\text{O})$	$0.716^{0.896}_{0.512}$	^{12}C(α, γ)^{16}O	+0.95	$0.731^{0.910}_{0.538}$	…	+0.95	(+25.1,−28.5) (+24.5,−26.3)
C-Depletion							
$M_{\text{ONe-Core}}$ ($M_\odot$)	$1.110^{1.365}_{0.550}$	^{12}C(^{12}C, p)^{23}Na	+0.58	$1.175^{1.444}_{0.575}$	…	+0.53	(+22.9,−50.5) (+22.9,−51.1)
$\tau_{\text{C-burn}}$ (kyr)	$30.74^{41.87}_{26.51}$	^{12}C(α, γ)^{16}O	+0.91	$23.75^{32.95}_{21.00}$	…	+0.94	(+0.78,−0.86) (+0.56,−0.62)
T_c (GK)	$1.158^{1.412}_{1.025}$	^{12}C(^{16}O, p)^{27}Al	−0.45	$1.196^{1.598}_{1.034}$	^{12}C(^{12}C, p)^{23}Na	−0.50	(+21.9,−11.5) (+33.6,−13.6)
ρ_c (10^6 g cm^{-3})	$5.317^{8.815}_{2.711}$	^{12}C(^{16}O, p)^{27}Al	−0.43	$4.371^{7.285}_{1.978}$	…	−0.43	(+65.8,−49.0) (+66.7,−54.8)
$Y_{e,c}$	$0.498^{0.499}_{0.497}$	^{12}C(α, γ)^{16}O	+0.72	$0.498^{0.500}_{0.497}$	…	+0.71	(+0.15,−0.35) (+0.15,−0.37)
$\xi_{2.5}$	$0.083^{0.095}_{0.069}$	^{12}C(α, γ)^{16}O	+0.49	$0.109^{0.129}_{0.088}$	^{12}C(^{12}C, p)^{23}Na	−0.54	(+14.28,−16.6) (+17.9,−19.4)
$X_c(^{16}\text{O})$	$0.622^{0.861}_{0.373}$	^{12}C(α, γ)^{16}O	+0.91	$0.625^{0.869}_{0.369}$	…	+0.88	(+38.4,−40.0) (+38.9,−41.0)
$X_c(^{20}\text{Ne})$	$0.266^{0.459}_{0.072}$	^{12}C(α, γ)^{16}O	−0.79	$0.280^{0.474}_{0.043}$	…	−0.75	(+72.4,−73.0) (+69.1,−84.5)
Ne-Depletion							
$M_{\text{ONe-Core}}$ ($M_\odot$)	$1.439^{2.368}_{1.113}$	^{12}C(^{12}C, p)^{23}Na	+0.82	$1.493^{1.965}_{1.157}$	…	+0.79	(+64.5,−22.7) (+31.6,−22.5)
$\tau_{\text{Ne-burn}}$ (yr)	$10.114^{44.452}_{0.493}$	^{12}C(α, γ)^{16}O	+0.91	$8.103^{37.39}_{0.143}$	…	+0.94	(+0.78,−0.86) (+0.56,−0.62)
T_c (GK)	$1.603^{1.702}_{1.501}$	^{12}C(α, γ)^{16}O	+0.80	$1.626^{1.727}_{1.520}$	…	+0.72	(+6.15,−6.40) (+6.21,−6.52)
ρ_c (10^6 g cm^{-3})	$5.119^{6.986}_{3.485}$	^{12}C(^{12}C, p)^{23}Na	+0.50	$4.422^{6.322}_{2.770}$	…	+0.52	(+36.5,−31.9) (+43.0,−37.4)
$Y_{e,c}$	$0.498^{0.499}_{0.496}$	^{12}C(α, γ)^{16}O	+0.59	$0.499^{0.500}_{0.497}$	…	+0.60	(+0.19,−0.41) (+0.19,−0.41)
$\xi_{2.5}$	$0.084^{0.101}_{0.068}$	^{12}C(α, γ)^{16}O	+0.71	$0.111^{0.136}_{0.084}$	^{12}C(^{12}C, p)^{23}Na	−0.57	(+20.2,−19.3) (+22.5,−24.4)
$X_c(^{16}\text{O})$	$0.731^{0.888}_{0.503}$	^{12}C(α, γ)^{16}O	+0.74	$0.735^{0.893}_{0.501}$	…	+0.70	(+21.4,−31.2) (+21.4,−31.8)
$X_c(^{28}\text{Si})$	$0.086^{0.240}_{0.021}$	^{12}C(α, γ)^{16}O	−0.62	$0.094^{0.296}_{0.018}$	…	−0.59	(+179,−75.2) (+216,−81.1)
O-Depletion							
$M_{\text{Ne-burn}}$ ($M_\odot$)	$0.270^{0.979}_{0.012}$	^{16}O(^{16}O,α)^{28}Si	+0.32	$0.219^{0.965}_{0.013}$	…	+0.21	(+262,−95.7) (+341,−94.2)
$\tau_{\text{O-burn}}$ (yr)	$3.786^{7.574}_{1.554}$	^{12}C(α, γ)^{16}O	+0.91	$2.348^{5.546}_{0.857}$	…	+0.93	(+0.76,−0.88) (+0.52,−0.61)
T_c (GK)	$2.073^{2.278}_{1.793}$	^{16}O(^{16}O, p)^{31}P	−0.56	$2.141^{2.350}_{1.860}$	…	−0.47	(+9.92,−13.5) (+9.77,−13.2)
ρ_c (10^6 g cm^{-3})	$23.34^{54.06}_{10.32}$	^{12}C(α, γ)^{16}O	−0.42	$15.10^{43.06}_{7.140}$	…	−0.38	(+132,−55.8) (+185,−52.7)
$Y_{e,c}$	$0.492^{0.498}_{0.479}$	^{16}O(^{16}O, n)^{31}S	−0.67	$0.493^{0.499}_{0.479}$	…	−0.71	(+1.18,−2.74) (+1.18,−2.88)
$\xi_{2.5}$	$0.102^{0.122}_{0.075}$	^{12}C(α, γ)^{16}O	+0.69	$0.139^{0.174}_{0.106}$	…	+0.51	(+19.9,−27.0) (+24.98,−23.6)
$X_c(^{28}\text{Si})$	$0.263^{0.526}_{0.106}$	^{16}O(^{16}O,α)^{28}Si	+0.39	$0.268^{0.544}_{0.111}$	^{16}O(^{16}O, p)^{31}P	−0.40	(+99.7,−59.8) (+103,−58.6)
$X_c(^{32}\text{S})$	$0.433^{0.736}_{0.058}$	^{16}O(^{16}O, p)^{31}P	+0.61	$0.449^{0.778}_{0.067}$	…	+0.59	(+70.1,−86.7) (+73.1,−85.1)

Note. Properties of the 15$M_\odot$ solar and subsolar stellar models at five different epochs. The values given are arithmetic means, with upper and lower limits from the 95% CI. Also listed are the minimum or maximum SROC coefficient values and the corresponding key nuclear reaction. The last column gives the limits of the 95% CI for the variations for the solar (left) and subsolar (right) stellar models. Ellipses indicate that the variation of a given quantity for the subsolar models is dominated by the same key reaction as for the solar models.

variations induced by uncertainties in nuclear reaction rates are of comparable magnitude to the variations induced by the modeling choices of mass resolution and network resolution. At Ne-depletion the integrated impact of the uncertainties in the reaction rates appears to be larger than the variations caused by mass and network resolution.

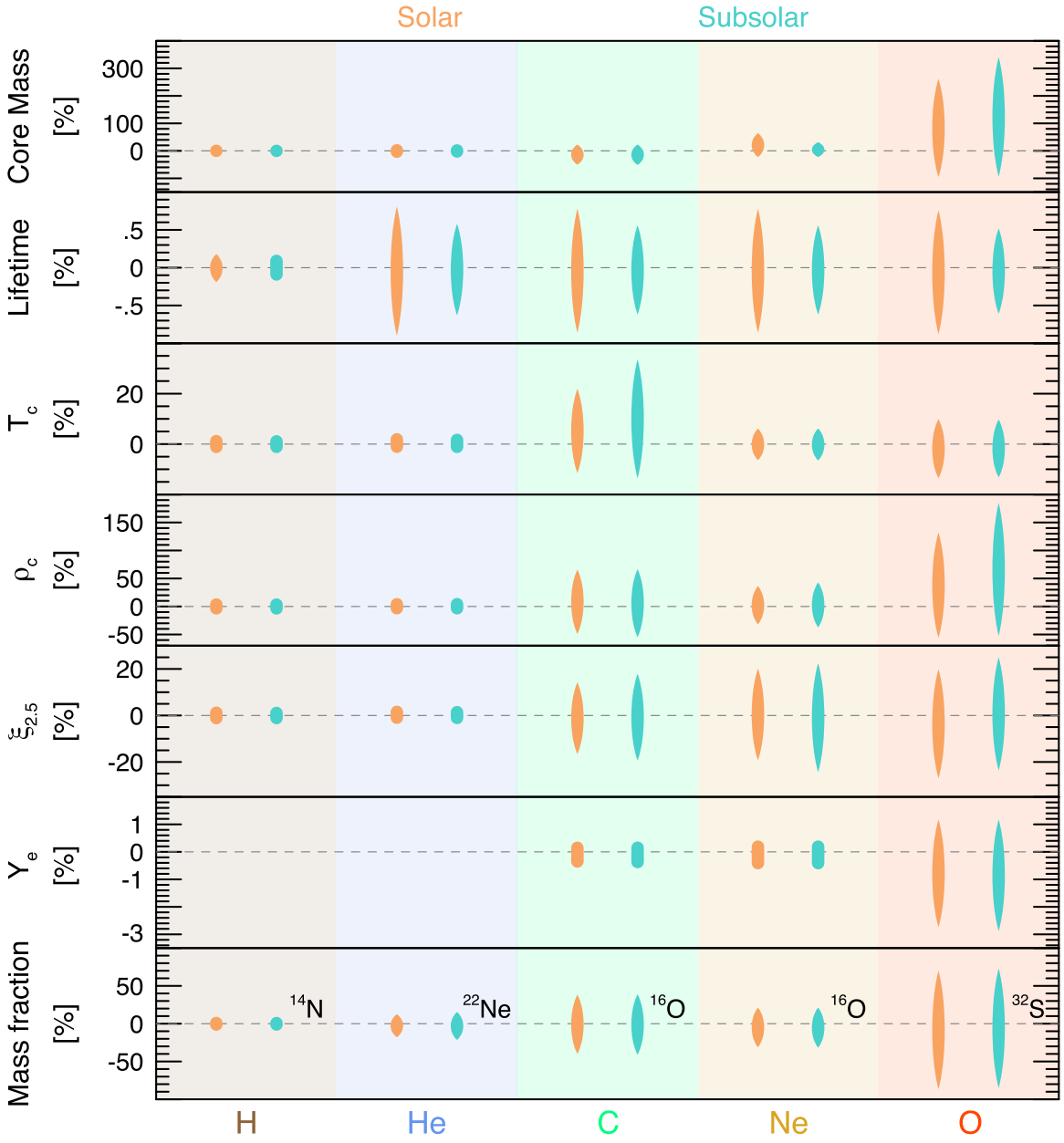

Figure 21. Percentage variations of the core mass, lifetime, central temperature, central density, compactness parameter, electron fraction, and a chosen "interesting" mass fraction (top to bottom) at H-, He-, C-, Ne-, and O-depletion (left to right). The vertical length of each tapered uncertainty band is the 95% CI for variations about the mean arithmetic value, listed in the last column of Table 1, and the horizontal width of each tapered uncertainty band schematically represents the underlying PDF. Solar metallicity models are shown by the orange bands and subsolar metallicity models by the green bands. The first occurrence of significant variation in the compactness parameter $\xi_{2.5}$ occurs at C-depletion. For the mass fractions, we choose to show $X_c(^{14}N)$ at H-depletion because it holds the star's initial CNO abundances, $X_c(^{22}Ne)$ at He-depletion because it holds the neutronization of the core, $X_c(^{16}O)$ at C- and Ne-depletion because it is the dominant nucleosynthesis product of massive stars, and $X_c(^{32}S)$ at O-depletion because it is a key component of the ashes of O-burning.

The variations due to different mass loss prescriptions and efficiencies were found to be of comparable scale to those due to reaction rate uncertainties at early epochs such as H- and He-depletion for the stellar properties considered. At early epochs, convective boundary mixing is likely to cause significant variations in core masses and lifetimes that are of larger scale than those due to nuclear reaction rate uncertainties. However, uncertainties in convective boundary mixing are likely to be smaller than the integrated impact of rate uncertainties at advanced burning stages.

7. Summary

We investigated properties of pre-supernova massive stars with respect to the composite uncertainties in the thermonuclear reaction rates by coupling the reaction rate PDFs provided by the STARLIB reaction rate library with MESA stellar models. We evolved 1000 $15M_{\odot}$ models with solar and subsolar initial compositions from the pre-main sequence to core oxygen depletion for a total of 2000 Monte Carlo stellar models. For each stellar model we sampled 665 forward thermonuclear reaction rates concurrently, and used them in an in situ

MESA reaction network of 127 isotopes. With this infrastructure we surveyed the core mass, burning lifetime, central temperature, central density, compactness parameter, and key abundances at H-, He-, C-, Ne-, and O-depletion.

At each stage, we measured the PDFs of the variations of each property and calculated SROC coefficients for each sampled reaction rate. This allowed identification of the reaction rates that have the largest impact on the variations of the properties surveyed. Table 1 summarizes the stellar properties, the reaction rates causing their variation, and the largest correlation coefficient (positive or negative) for that reaction rate.

In general, variations induced by nuclear reaction rates grow with each passing phase of evolution. We found that variations induced by uncertainties in nuclear reaction rates at core H- and He-depletion are of comparable magnitude to the variations induced by the modeling choices of mass resolution and the number of isotopes in the nuclear reaction network. Beyond these evolutionary epochs, our models suggest that the reaction rate uncertainties can dominate the variation in properties of the stellar model significantly, altering the evolution toward iron core-collapse.

This project was supported by NSF under the *Software Infrastructure for Sustained Innovation* (SI2) program grants (ACI-1339581, ACI-1339600, ACI-1339606, ACI-1663684, ACI-1663688, ACI-1663696) and grant PHY-1430152 for the *Physics Frontier Center* "Joint Institute for Nuclear Astrophysics—Center for the Evolution of the Elements" (JINA-CEE). This project was also supported by NASA under the *Theoretical and Computational Astrophysics Networks* (TCAN) program grants (NNX14AB53G, NNX14AB55G, NNX12AC72G) and the Astrophysics Theory Program grant 14-ATP14-0007. C.E.F. acknowledges support from a Predoctoral Fellowship administered by the National Academies of Sciences, Engineering, and Medicine on behalf of the Ford Foundation, an Edward J Petry Graduate Fellowship from Michigan State University, and the National Science Foundation Graduate Research Fellowship Program under grant number DGE1424871. S.M.C. is supported by the U.S. Department of Energy, Office of Science, Office of Nuclear Physics, under Award Numbers DE-SC0015904 and DE-SC0017955, the Research Corporation for Science Advancement under Scialog Grant 23770, and the *Chandra* X-ray Observatory under grant TM7-18005X. The simulations presented in this work were performed on the laconia cluster supported by the Institute for Cyber-Enabled Research (ICER) at Michigan State University. This research made extensive use of the SAO/NASA Astrophysics Data System (ADS).

Software: MESA (Paxton et al. 2011, 2013, 2015), STARLIB (Sallaska et al. 2013; Iliadis et al. 2015, 2016, http://starlib.physics.unc.edu), Python available from http://www.python.org, matplotlib (Hunter 2007), NumPy (van der Walt et al. 2011), and scipy (Jones et al. 2001).

ORCID iDs

C. E. Fields https://orcid.org/0000-0002-8925-057X
F. X. Timmes https://orcid.org/0000-0002-0474-159X
R. Farmer https://orcid.org/0000-0003-3441-7624
I. Petermann https://orcid.org/0000-0003-2434-1128
William M. Wolf https://orcid.org/0000-0002-6828-0630
S. M. Couch https://orcid.org/0000-0002-5080-5996

References

Abbott, B. P., Abbott, R., Abbott, T. D., et al. 2016a, PhRvL, 116, 061102
Abbott, B. P., Abbott, R., Abbott, T. D., et al. 2016b, PhRvL, 116, 241103
Abbott, B. P., Abbott, R., Abbott, T. D., et al. 2017, PhRvL, 118, 221101
Alastuey, A., & Jancovici, B. 1978, ApJ, 226, 1034
Angulo, C., Arnould, M., Rayet, M., et al. 1999, NuPhA, 656, 3
Asplund, M., Grevesse, N., Sauval, A. J., & Scott, P. 2009, ARA&A, 47, 481
Barkat, Z., Rakavy, G., & Sack, N. 1967, PhRvL, 18, 379
Bennett, M. E., Hirschi, R., Pignatari, M., et al. 2012, MNRAS, 420, 3047
Bromm, V., Kudritzki, R. P., & Loeb, A. 2001, ApJ, 552, 464
Brown, J. M., Garaud, P., & Stellmach, S. 2013, ApJ, 768, 34
Caffau, E., Ludwig, H.-G., Bonifacio, P., et al. 2010, A&A, 514, A92
Carnelli, P. F. F., Almaraz-Calderon, S., Rehm, K. E., et al. 2014, PhRvL, 112, 192701
Caughlan, G. R., & Fowler, W. A. 1988, ADNDT, 40, 283
Chatzopoulos, E., Couch, S. M., Arnett, W. D., & Timmes, F. X. 2016a, ApJ, 822, 61
Chatzopoulos, E., & Wheeler, J. C. 2012, ApJ, 748, 42
Chatzopoulos, E., Wheeler, J. C., & Couch, S. M. 2013, ApJ, 776, 129
Chatzopoulos, E., Wheeler, J. C., Vinko, J., et al. 2016b, ApJ, 828, 94
Chen, K.-J., Woosley, S. E., & Sukhbold, T. 2016, ApJ, 832, 73
Clausen, D., Piro, A. L., & Ott, C. D. 2015, ApJ, 799, 190
Côté, B., O'Shea, B. W., Ritter, C., Herwig, F., & Venn, K. A. 2017, ApJ, 835, 128
Couch, S. M., Chatzopoulos, E., Arnett, W. D., & Timmes, F. X. 2015, ApJL, 808, L21
Cristini, A., Meakin, C., Hirschi, R., et al. 2017, MNRAS, 471, 279
Cyburt, R. H., Amthor, A. M., Ferguson, R., et al. 2010, ApJS, 189, 240
Cyburt, R. H., Amthor, A. M., Heger, A., et al. 2016, ApJ, 830, 55
Daigle, S., Kelly, K. J., Champagne, A. E., et al. 2016, PhRvC, 94, 025803
Davis, A., Jones, S., & Herwig, F. 2017, arXiv:1712.00114
deBoer, R. J., Görres, J., Wiescher, M., et al. 2017, RvMP, 89, 035007
Dessart, L., Hillier, D. J., Livne, E., et al. 2011, MNRAS, 414, 2985
Dong, S., Shappee, B. J., Prieto, J. L., et al. 2016, Sci, 351, 257
Eldridge, J. J., & Tout, C. A. 2004, MNRAS, 353, 87
Evans, M., Hastings, N., & Peacock, B. 2000, Statistical Distributions (3rd ed.; New York: Wiley)
Fang, X., Tan, W. P., Beard, M., et al. 2017, PhRvC, 96, 045804
Farmer, R., Fields, C. E., Petermann, I., et al. 2016, ApJS, 227, 22
Farmer, R., Fields, C. E., & Timmes, F. X. 2015, ApJ, 807, 184
Faulkner, J. 1967, ApJ, 147, 617
Fields, C. E., Farmer, R., Petermann, I., Iliadis, C., & Timmes, F. X. 2016, ApJ, 823, 46
Filippenko, A. V. 1997, ARA&A, 35, 309
Fowler, W. A., & Hoyle, F. 1964, ApJS, 9, 201
Fraley, G. S. 1968, Ap&SS, 2, 96
Frebel, A., Simon, J. D., Geha, M., & Willman, B. 2010, ApJ, 708, 560
Fryer, C. L., & Kalogera, V. 2001, ApJ, 554, 548
Fryer, C. L., Woosley, S. E., & Heger, A. 2001, ApJ, 550, 372
Fuller, G. M., Fowler, W. A., & Newman, M. J. 1985, ApJ, 293, 1
Garaud, P., Medrano, M., Brown, J. M., Mankovich, C., & Moore, K. 2015, ApJ, 808, 89
Gasques, L. R., Brown, E. F., Chieffi, A., et al. 2007, PhRvC, 76, 035802
Glebbeek, E., Gaburov, E., de Mink, S. E., Pols, O. R., & Portegies Zwart, S. F. 2009, A&A, 497, 255
Gómez Iñesta, Á, Iliadis, C., & Coc, A. 2017, arXiv:1710.01647
Goriely, S., Hilaire, S., & Koning, A. J. 2008, A&A, 487, 767
Grevesse, N., & Sauval, A. J. 1998, SSRv, 85, 161
Hansen, C. J., Kawaler, S. D., & Trimble, V. 2004, Stellar Interiors : Physical Principles, Structure, and Evolution (New York: Springer)
Harris, J. A., Hix, W. R., Chertkow, M. A., et al. 2017, ApJ, 843, 2
Heger, A., Fryer, C. L., Woosley, S. E., Langer, N., & Hartmann, D. H. 2003, ApJ, 591, 288
Herwig, F., Austin, S. M., & Lattanzio, J. C. 2006, PhRvC, 73, 025802
Hoyle, F., & Lyttleton, R. A. 1942, MNRAS, 102, 177
Hunter, J. D. 2007, CSE, 9, 90
Iben, I., Jr. 1966, ApJ, 143, 516
Iben, I., Jr. 1991, ApJS, 76, 55
Iliadis, C. 2007, Nuclear Physics of Stars (New York: Wiley-VCH)
Iliadis, C., Anderson, K. S., Coc, A., Timmes, F. X., & Starrfield, S. 2016, ApJ, 831, 107
Iliadis, C., Longland, R., Champagne, A. E., & Coc, A. 2010, NuPhA, 841, 251
Iliadis, C., Longland, R., Coc, A., Timmes, F. X., & Champagne, A. E. 2015, JPhG, 42, 034007

Imbriani, G., Costantini, H., Formicola, A., et al. 2004, A&A, 420, 625
Imbriani, G., Costantini, H., Formicola, A., et al. 2005, EPJA, 25, 455
Itoh, N., Hayashi, H., Nishikawa, A., & Kohyama, Y. 1996, ApJS, 102, 411
Itoh, N., Totsuji, H., Ichimaru, S., & Dewitt, H. E. 1979, ApJ, 234, 1079
Janka, H.-T., Melson, T., & Summa, A. 2016, arXiv:1602.05576
Jerkstrand, A., Timmes, F. X., Magkotsios, G., et al. 2015, ApJ, 807, 110
Jiang, C. L., Back, B. B., Janssens, R. V. F., & Rehm, K. E. 2007a, PhRvC, 75, 057604
Jiang, C. L., Rehm, K. E., Back, B. B., & Janssens, R. V. F. 2007b, PhRvC, 75, 015803
Jones, E., Oliphant, T., Peterson, P., et al. 2001, SciPy: Open Source Scientific Tools for Python, Online, SciPy, http://www.scipy.org/
Jones, S., Andrassy, R., Sandalski, S., et al. 2017, MNRAS, 465, 2991
Karakas, A. I., & Lattanzio, J. C. 2014, PASA, 31, 30
Kasen, D., Woosley, S. E., & Heger, A. 2011, ApJ, 734, 102
Kruckow, M. U., Tauris, T. M., Langer, N., et al. 2016, A&A, 596, A58
Kunz, R., Fey, M., Jaeger, M., et al. 2002, ApJ, 567, 643
Lamb, S. A., Iben, I., Jr., & Howard, W. M. 1976, ApJ, 207, 209
Lane, D. 2013, Online Statistics Education: A Multimedia Course of Study. Rice University, http://onlinestatbook.com
Langanke, K., & Martínez-Pinedo, G. 2000, NuPhA, 673, 481
Leloudas, G., Fraser, M., Stone, N. C., et al. 2016, NatAs, 1, 0002
LUNA Collaboration, Lemut, A., Bemmerer, D., et al. 2006, PhLB, 634, 483
Limongi, M. 2017, arXiv:1706.01913
Lodders, K., Palme, H., & Gail, H.-P. 2009, LanB, 4B, 44
Longland, R. 2012, A&A, 548, A30
Longland, R., Iliadis, C., Champagne, A. E., et al. 2010, NuPhA, 841, 1
Magkotsios, G., Timmes, F. X., Hungerford, A. L., et al. 2010, ApJS, 191, 66
Martínez-Rodríguez, H., Badenes, C., Yamaguchi, H., et al. 2017, ApJ, 843, 35
Mişicu, Ş, & Esbensen, H. 2007, PhRvC, 75, 034606
Müller, B., Heger, A., Liptai, D., & Cameron, J. B. 2016, MNRAS, 460, 742
Myers, J. L., & Well, A. D. 1995, Research Design & Statistical Analysis (1st ed.; Abingdon: Routledge)
Nguyen, N. B., Nunes, F. M., Thompson, I. J., & Brown, E. F. 2012, PhRvL, 109, 141101
Nieuwenhuijzen, H., & de Jager, C. 1990, A&A, 231, 134
Nishimura, N., Hirschi, R., Rauscher, T., Murphy, A. S. J., & Cescutti, G. 2017, MNRAS, 469, 1752
Nomoto, K., Kobayashi, C., & Tominaga, N. 2013, ARA&A, 51, 457
Nugis, T., & Lamers, H. J. G. L. M. 2000, A&A, 360, 227
Ober, W. W., El Eid, M. F., & Fricke, K. J. 1983, A&A, 119, 61
O'Connor, E., & Ott, C. D. 2011, ApJ, 730, 70
Oda, T., Hino, M., Muto, K., Takahara, M., & Sato, K. 1994, ADNDT, 56, 231
Ofek, E. O., Sullivan, M., Shaviv, N. J., et al. 2014, ApJ, 789, 104
Pagel, B. E. J., & Portinari, L. 1998, MNRAS, 298, 747
Paxton, B., Bildsten, L., Dotter, A., et al. 2011, ApJS, 192, 3
Paxton, B., Cantiello, M., Arras, P., et al. 2013, ApJS, 208, 4
Paxton, B., Marchant, P., Schwab, J., et al. 2015, ApJS, 220, 15
Pignatari, M., Hirschi, R., Wiescher, M., et al. 2013, ApJ, 762, 31
Portinari, L., Casagrande, L., & Flynn, C. 2010, MNRAS, 406, 1570
Rakavy, G., & Shaviv, G. 1967, ApJ, 148, 803
Rakavy, G., Shaviv, G., & Zinamon, Z. 1967, ApJ, 150, 131
Rauscher, T., Heger, A., Hoffman, R. D., & Woosley, S. E. 2002, ApJ, 576, 323
Rauscher, T., Nishimura, N., Hirschi, R., et al. 2016, MNRAS, 463, 4153
Reilly, E., Maund, J. R., Baade, D., et al. 2016, MNRAS, 457, 288
Renzo, M., Ott, C. D., Shore, S. N., & de Mink, S. E. 2017, A&A, 603, A118
Sallaska, A. L., Iliadis, C., Champange, A. E., et al. 2013, ApJS, 207, 18
Salpeter, E. E. 1955, ApJ, 121, 161
Scalo, J. M. 1986, FCPh, 11, 1
Smartt, S. J. 2009, ARA&A, 47, 63
Smartt, S. J. 2015, PASA, 32, 16
Smith, N. 2014, ARA&A, 52, 487
Smith, N., Andrews, J. E., Van Dyk, S. D., et al. 2016, MNRAS, 458, 950
Spruit, H. C. 2013, A&A, 552, A76
Stancliffe, R. J., Chieffi, A., Lattanzio, J. C., & Church, R. P. 2009, PASA, 26, 203
Sukhbold, T., Ertl, T., Woosley, S. E., Brown, J. M., & Janka, H.-T. 2016, ApJ, 821, 38
Sukhbold, T., Woosley, S., & Heger, A. 2017, arXiv:1710.03243
Sukhbold, T., & Woosley, S. E. 2014, ApJ, 783, 10
Sukhbold, T., & Woosley, S. E. 2016, ApJL, 820, L38
Timmes, F. X., Woosley, S. E., & Weaver, T. A. 1996, ApJ, 457, 834
Traxler, A., Garaud, P., & Stellmach, S. 2011, ApJ, 728, L29
Ugliano, M., Janka, H.-T., Marek, A., & Arcones, A. 2012, ApJ, 757, 69
Vagnozzi, S., Freese, K., & Zurbuchen, T. H. 2017, ApJ, 839, 55
van der Walt, S., Colbert, S. C., & Varoquaux, G. 2011, CSE, 13, 22
Van Dyk, S. D., Peng, C. Y., King, J. Y., et al. 2000, PASP, 112, 1532
Vink, J. S., de Koter, A., & Lamers, H. J. G. L. M. 2001, A&A, 369, 574
Wang, L., & Wheeler, J. C. 2008, ARA&A, 46, 433
Weiss, A., Serenelli, A., Kitsikis, A., Schlattl, H., & Christensen-Dalsgaard, J. 2005, A&A, 441, 1129
West, C., & Heger, A. 2013, ApJ, 774, 75
West, C., Heger, A., & Austin, S. M. 2013, ApJ, 769, 2
Woosley, S. E. 2016, ApJL, 824, L10
Woosley, S. E. 2017, ApJ, 836, 244
Woosley, S. E., Arnett, W. D., & Clayton, D. D. 1971, PhRvL, 27, 700
Woosley, S. E., & Heger, A. 2007, PhR, 442, 269
Woosley, S. E., Heger, A., & Weaver, T. A. 2002, RvMPh, 74, 1015
Woosley, S. E., & Weaver, T. A. 1986, ARA&A, 24, 205
Xu, Y., Takahashi, K., Goriely, S., et al. 2013, NuPhA, 918, 61
Zaussinger, F., & Spruit, H. C. 2013, A&A, 554, A119
Zhang, W., Woosley, S. E., & Heger, A. 2008, ApJ, 679, 639